Mechanisms underlying Myosin 10's contribution to the maintenance of mitotic spindle bipolarity

Yang-In Yim[a], Antonio Pedrosa[a], Xufeng Wu[a], Krishna Chinthalapudi[b], Richard E. Cheney[c], and John A. Hammer[a,*]

[a]Cell and Developmental Biology Center, National Heart, Lung and Blood Institute, National Institutes of Health, Bethesda, MD 20892; [b]Department of Physiology and Cell Biology, College of Medicine, The Ohio State University, Columbus, OH 43210; [c]Department of Cell Biology and Physiology, University of North Carolina, Chapel Hill, NC 27599

ABSTRACT **Myosin 10 (Myo10) couples microtubules and integrin-based adhesions to movement along actin filaments via its microtubule-binding MyTH4 domain and integrin-binding FERM domain, respectively. Here we show that Myo10-depleted HeLa cells and mouse embryo fibroblasts (MEFs) both exhibit a pronounced increase in the frequency of multipolar spindles. Staining of unsynchronized metaphase cells showed that the primary driver of spindle multipolarity in Myo10-depleted MEFs and in Myo10-depleted HeLa cells lacking supernumerary centrosomes is pericentriolar material (PCM) fragmentation, which creates γ-tubulin-positive acentriolar foci that serve as extra spindle poles. For HeLa cells possessing supernumerary centrosomes, Myo10 depletion further accentuates spindle multipolarity by impairing the clustering of the extra spindle poles. Complementation experiments show that Myo10 must interact with both microtubules and integrins to promote PCM/pole integrity. Conversely, Myo10 only needs interact with integrins to promote supernumerary centrosome clustering. Importantly, images of metaphase Halo–Myo10 knockin cells show that the myosin localizes exclusively to the spindle and the tips of adhesive retraction fibers. We conclude that Myo10 promotes PCM/pole integrity in part by interacting with spindle microtubules, and that it promotes supernumerary centrosome clustering by supporting retraction fiber-based cell adhesion, which likely serves to anchor the microtubule-based forces driving pole focusing.**

SIGNIFICANCE STATEMENT

- Multipolar spindles often lead to aneuploidy.
- Here we show that myosin 10 (Myo10) depleted cells exhibit an increase in the frequency of multipolar spindles due to PCM/pole fragmentation and to decreased clustering of supernumerary centrosomes. Endogenously tagged myo10 localizes exclusively to the spindle and the tips of retraction fibers supporting integrin-based adhesion during mitosis.
- Consistently, myo10's ability to promote the clustering of supernumerary centrosomes, a process used by many cancer cell types to avoid aneuploidy, depends on its ability to interact with integrins. Drugs that block this interaction could serve as cancer therapeutics.

Monitoring Editor
Thomas Pollard
Yale University

Received: Jul 24, 2023
Revised: Nov 13, 2023
Accepted: Nov 17, 2023

This article was published online ahead of print in MBoC in Press (http://www.molbiolcell.org/cgi/doi/10.1091/mbc.E23-07-0282) on November 29, 2023.

*Address correspondence to: John A. Hammer (hammerj@nhlbi.nih.gov).

Abbreviations used: cKO, conditional knockout; EGTA, ethylene glycol-bis(β-aminoethyl ether)-*N,N,N′,N′*-tetraacetic acid; KD, knockdown; KI, knockin; KO, knockout; MEF, mouse embryo fibroblast; MTOC, microtubule organizing center; Myo10, myosin 10; PCM, pericentriolar material; PFA, paraformaldehyde; WT, wild type.

INTRODUCTION

Myosin 10 (Myo10) is a member of the MyTH4/FERM domain family of unconventional myosins (reviewed in Sousa and Cheney, 2005; Kerber and Cheney, 2011; Weck *et al.*, 2017; Tokuo, 2020; Houdusse and Titus, 2021). These actin-based motors are special in that they can interact with microtubules and integrins via their MyTH4 and FERM domains, respectively. Myo10 is known as the "filopodial myosin" because it accumulates dramatically at the tips of filopodia (Berg *et al.*, 2000; Berg and Cheney, 2002; Pi *et al.*, 2007), and because cells that overexpress or lack Myo10 exhibit increases and decreases in filopodia number, respectively (Berg and Cheney, 2002; Bohil *et al.*, 2006; Tokuo *et al.*, 2007; Plantard *et al.*, 2010; Singh *et al.*, 2010; Raines *et al.*, 2012; He *et al.*, 2017; Heimsath *et al.*, 2017; Horsthemke *et al.*, 2017; Alieva *et al.*, 2019; Hammers *et al.*, 2021). Consistent with these observations, Myo10 prefers to walk on bundled actin filaments like those that comprise filopodia (Nagy *et al.*, 2008; Ricca and Rock, 2010; Ropars *et al.*, 2016), and it can be seen to move out filopodia at ~800 nm/s (Berg and Cheney, 2002; Kerber *et al.*, 2009). Perhaps most importantly for this study, Myo10 promotes the formation of adhesions within filopodia by virtue of its FERM domain-dependent binding to β1-integrin (Zhang *et al.*, 2004; Hirano *et al.*, 2011; Miihkinen *et al.*, 2021). These filopodial adhesions can sense extracellular matrix (ECM) stiffness and topography (Morgan *et al.*, 2009; Albuschies and Vogel, 2013; Wong *et al.*, 2014; Johnson *et al.*, 2015), generate traction force (Morgan *et al.*, 2009; Romero *et al.*, 2012; Albuschies and Vogel, 2013; Bornschlögl *et al.*, 2013; Lagarrigue *et al.*, 2015; Leijnse *et al.*, 2015; Alieva *et al.*, 2019), and often mature into focal adhesions upon cell advance (Schäfer *et al.*, 2009; Hu *et al.*, 2014; Wong *et al.*, 2014; Johnson *et al.*, 2015; Jacquemet *et al.*, 2016, 2019; Fischer *et al.*, 2019). Consistently, Myo10-dependent filopodial adhesions have been implicated in cell migration and cancer cell metastasis (reviewed in Jacquemet *et al.*, 2015; Alieva *et al.*, 2019; Gallop, 2020).

While the bulk of cell biological studies to date have focused on Myo10's role in the structure and function of filopodia, which are generally devoid of microtubules, Myo10 also plays important roles in microtubule-dependent processes. The best evidence for this has come from studies focusing on Myo10's role in meiosis and mitosis. First, Weber and colleagues (2004) showed that an antiMyo10 antibody stains the portion of the frog egg meiotic spindle in contact with the actin cortex, and that disrupting Myo10 function via expression of a dominant negative construct or microinjection of the anti-Myo10 antibody inhibits nuclear anchoring, spindle assembly, and spindle-cortex association in eggs. Subsequently, Woolner and colleagues (2008) showed that the antiMyo10 antibody stains spindles and spindle poles in embryonic frog epithelial cells, and that morpholino-based partial knockdown (KD) of Myo10 causes defects in spindle anchoring, spindle length, spindle dynamics, and metaphase progression. They also showed that about 15% of spindle poles in Myo10 morphants fragment during early anaphase, leading to multipolar spindles (Woolner *et al.*, 2008). While the extent to which this apparent defect in pole stability was due to centriole disengagement versus PCM fragmentation was not determined, and while a requirement for MyTH4 domain: microtubule interaction was not demonstrated for any of the phenotypes, Woolner and colleagues (2008) did show that Myo10's isolated MyTH4/FERM domain interacts with the pole factor TPX2, and that Myo10 is required for the robust localization of TPX2 at and near poles. Based on these findings, they argued that Myo10 maintains spindle pole integrity by recruiting TPX2, and that, without the stabilizing effect of TPX2, poles in Myo10 KD cells tend to fragment when subjected to the strong chromosomal and spindle forces that ramp up during metaphase.

In a more recent study, Kwon and colleagues (2015) presented evidence that Myo10 also plays a role in positioning the mitotic spindle. These authors used overexpression of GFP-tagged Myo10 and RNAi-mediated KD to show that the myosin localizes to subcortical actin clouds at the equator of dividing HeLa cells where it cooperates in a nonredundant manner with cortical dynein to position the mitotic spindle. Importantly, the positioning defect exhibited by Myo10 KD cells was not rescued by a version of Myo10 harboring a mutated MyTH4 domain that can no longer bind to microtubules, arguing that the myosin must be capable of interacting with microtubules to assist in spindle positioning. That said, Toyoshima and Nishida (2007) showed that the ability of integrin-based adhesions to orient the mitotic spindle parallel to the substratum requires Myo10. This result suggests that Myo10 might promote spindle positioning at least in part through its FERM domain-dependent interaction with integrins, although this possibility was not explored. In a subsequent study, however, Iwano and colleagues (2015) presented evidence the that cyclin-dependent kinase PCTK1 phosphorylates KAP0, a regulatory subunit of protein kinase A, that phospho-KAP0 binds to the FERM domain of Myo10 to enhance its interaction with integrin, and that this enhancement facilitates the retraction fiber-dependent control of spindle orientation (Thery and Bornens, 2006; Théry *et al.*, 2007).

Finally, Myo10 has been implicated along with the pole focusing, microtubule minus end-directed kinesin 14 family member HSET in the clustering of the extra spindle poles that appear in cells exhibiting supernumerary centrosomes during interphase (Kwon *et al.*, 2008). This process, which is usually referred to as supernumerary centrosome clustering, serves to cluster the extra spindle poles into two groups to enable a bipolar mitosis. Myo10 may cooperate with HSET to promote the clustering of supernumerary centrosomes in a manner similar to how Kwon *et al.* (2015) argue it cooperates with cortical dynein to position the mitotic spindle, as Myo10 with a mutated MyTH4 domain could not rescue the multipolar phenotype exhibited by Myo10 KD cells over overexpressing PLK4. Whether Myo10 must also interact with integrins via its FERM domain to promote supernumerary centrosome clustering has not been tested.

Here we used two genome-edited HeLa cell clones that are almost devoid of Myo10 and MEFs isolated from our Myo10 knockout (KO) mouse (Heimsath *et al.*, 2017) to define the contribution that Myo10 makes to maintaining spindle bipolarity. We then used complementation of the Myo10-depleted HeLa cells with mutated versions of Myo10 to quantitate the contributions that its microtubule-binding MyTH4 and integrin-binding FERM domains make to the myosin's ability to maintain spindle bipolarity. Finally, we used HeLa cells in which one Myo10 allele was tagged with Halo using CRISPR to obtain definitive information on the myosin's localization during mitosis. This approach may be particularly important as Myo10 is a low abundance protein (Kerber and Cheney, 2011), making localizations based on over expression problematic. We find that both Myo10 depleted cell types exhibit a pronounced increase in the frequency of multipolar spindles, and that two separate defects related to spindle pole biology are responsible. The first defect, spindle pole fragmentation, is the major driver of multipolar spindles in KO MEFs and in Myo10-depleted HeLa cells lacking supernumerary centrosomes. We show that pole fragmentation is due almost entirely to PCM fragmentation (centriole disengagement plays a minor role), and that fragmentation occurs as cells approach metaphase, arguing that it is force-dependent. We do not, however, see defects in the recruitment of either TPX2 or the pole maturation marker CDK5Rap2. Moreover, we do not see Myo10 at poles in Halo–Myo10 knockin (KI)

cells. We do, however, see Myo10 in the spindle, but only if it harbors a functional, microtubule-binding MyTH4 domain. Finally, complementation shows that the Myo10 must interact with both integrins and microtubules to promote pole stability. Together, these results indicate that the defect in PCM integrity is not a direct result of losing Myo10 at spindle poles, nor is it due to a general defect in spindle pole maturation. Instead, our results suggest that Myo10 promotes PCM/pole integrity at least in part through a MyTH4 domain-dependent interaction with spindle microtubules.

The second defect, an inability to cluster extra spindle poles, is the major driver of multipolar spindles in Myo10-depleted HeLa cells possessing supernumerary centrosomes. Unlike the defect in PCM/pole stability, Myo10 only needs interact with integrins to promote supernumerary centrosome clustering. Consistently, endogenously tagged Myo10 localizes dramatically to the tips of retraction fibers, which are known to support integrin-based adhesion during mitosis (Mitchison, 1992; Cramer and Mitchison, 1993, 1995, 1997; Dix *et al.*, 2018; Taubenberger *et al.*, 2020). These and other results argue that Myo10 promotes supernumerary centrosome clustering primarily by promoting retraction fiber-based cell adhesion, which likely serves as one of several anchors required for the efficient focusing of supernumerary poles by microtubule-based forces (Krämer *et al.*, 2011).

RESULTS

Myo10-depleted HeLa cells exhibit a pronounced increase in the frequency of multipolar spindles

We used CRISPR-Cas9-based genome editing in an effort to abrogate Myo10 expression in HeLa cells, which are polyploid and contain three Myo10 alleles based on chromosomal duplications (Beskow, 2016). Guide RNAs targeting the sequence encoding residues 57 to 62 in the 2058-residue human myo10 heavy chain was introduced into cells by electroporation. Single cell sorting of GFP-positive cells yielded only two putative Myo10 KO clones (KO-1 and KO-2) from 384 wells. This low number likely reflects stresses incurred by single-cell sorting, the mitotic defects that occur when Myo10 is depleted, and the fact that these defects are more pronounced at lower cell densities (see below). Sequencing of PCR products that span the gRNA sequence revealed no WT sequence, two frameshift mutations and one missense mutation in both KO-1 and KO-2, with the latter causing six and five residue in-frame deletions in KO-1 and KO-2, respectively (see *Materials and Methods* for additional details). Consistently, Western blots revealed a large reduction in Myo10 levels in KO-1 and KO-2 (Figure 1A), with scans showing that they contain 7.1 and 13.8% of normal Myo10 levels, respectively (Supplemental Figure S1A). We conclude, therefore, that both KO-1 and KO-2 contain no WT alleles, two nonsense/null alleles and one missense allele, making them hypomorphs that express minor amounts of Myo10 containing small deletions within the motor domain that might compromise function. While not complete KOs, we refer to these two genome-edited HeLa cell lines as KO-1 and KO-2 for the sake of simplicity.

To identify possible defects in mitotic spindle organization upon Myo10 depletion, we fixed and stained WT HeLa, KO-1, and KO-2 for γ-tubulin to label spindle poles, α-tubulin to label spindle microtubules, and DAPI to label chromosomes. Importantly, all spindle scoring was done using unsynchronized cells, as synchronization treatments such as low dose nocodazole can lead to the formation of multipolar spindles with abnormal centriole distributions due to cohesion fatigue (Maiato and Logarinho, 2014). Metaphase cells were optically sectioned in 0.25-μm intervals, and the sections used to count spindle pole numbers and to determine spindle and chromosome organization in three-dimensional. Cells were scored as being either bipolar (cells with just two spindle poles, one at each end of a normal bipolar spindle, and pseudobipolar cells, where one or both poles of a normal looking bipolar spindle were created by the clustering of supernumerary centrosomes; Figure 1, E1–E4; Z-Stack Movie 1), semipolar (cells possessing two major poles and a normal looking spindle, but also a minor pole in a different focal plane that contributed some microtubules to the spindle; Figure 1, F1–F4; Z-Stack Movie 2), or multipolar (cells with more than two major spindle poles; Figure 1, G1–G4; Z-Stack Movie 3). Scoring showed that KO-1 and KO-2 exhibit 11.8 and 22.7% decreases in the frequency of bipolar spindles (Figure 1, H and I1), 3.2-fold and 5.0-fold increases in the frequency of multipolar spindles (Figure 1, H and I2), and 2.6-fold and 3.9-fold increases in the frequency of nonbipolar spindles (semipolar plus multipolar; Figure 1, H and I3), respectively. We conclude, therefore, that HeLa cells with greatly reduced levels of Myo10 exhibit a pronounced increase in the frequency of multipolar spindles.

Myo10-depleted HeLa cells exhibit an increase in the frequency of spindles that are not parallel to the substratum

For cells dividing in two-dimensions, the balance of forces driving spindle positioning are such that the spindle's long axis is usually parallel to the substratum, resulting in the two poles being equidistant from the substratum that is, in the same Z-plane. Optical sectioning of metaphase cells exhibiting just two poles showed that the average distance in Z separating the two spindle poles was significantly greater in both KO lines (Figure 2A; Figure 2D shows the distributions of these distances in 1-μm intervals; see also Z-Stack Movie 4). This phenotype could reflect a defect in the adhesion of Myo10 depleted cells, resulting in an imbalance in the pulling forces driving spindle positioning (Toyoshima and Nishida, 2007). While the mean values for the separation of the two poles in Z was also elevated in both KO lines at anaphase and telophase (Figure 2, B and C; Z-Stack Movies 5 and 6), the differences were not quite statistically significant at anaphase and far from significant at telophase. This result indicates that the defect in positioning the metaphase spindle relative to the substratum when Myo10 is depleted is largely corrected as cells approach telophase.

Myo10-depleted HeLa cells exhibit increased frequencies of chromosome misalignment and lagging chromosomes

Cells with multipolar or improperly positioned spindles often exhibit chromosome misalignment at metaphase and lagging chromosomes later in mitosis due to merotelic or missing kinetochore attachments. Imaging of mitotic cells between metaphase and telophase following fixation and staining for DNA, microtubules and spindle poles revealed evidence of these chromosome distribution defects in Myo10 depleted cells undergoing both bipolar and multipolar divisions (Figure 2, E1–E6; the arrows in E3–E6 indicate lagging chromosomes). Indeed, scoring showed that the percentage of mitotic cells exhibiting chromosome misalignment and/or lagging chromosomes was 4.0- and 4.5-fold higher in KO-1 and KO-2, respectively (Figure 2F). This result is consistent with the defects in spindle bipolarity and spindle positioning exhibited by these two Myo10-depleted HeLa cell lines.

HeLa cells in which Myo10 levels were reduced using siRNA also exhibit an increase in the frequency of multipolar spindles

KO-1 and KO-2 initially grew very slowly, only approaching an approximately normal growth rate after about 2 mo in culture

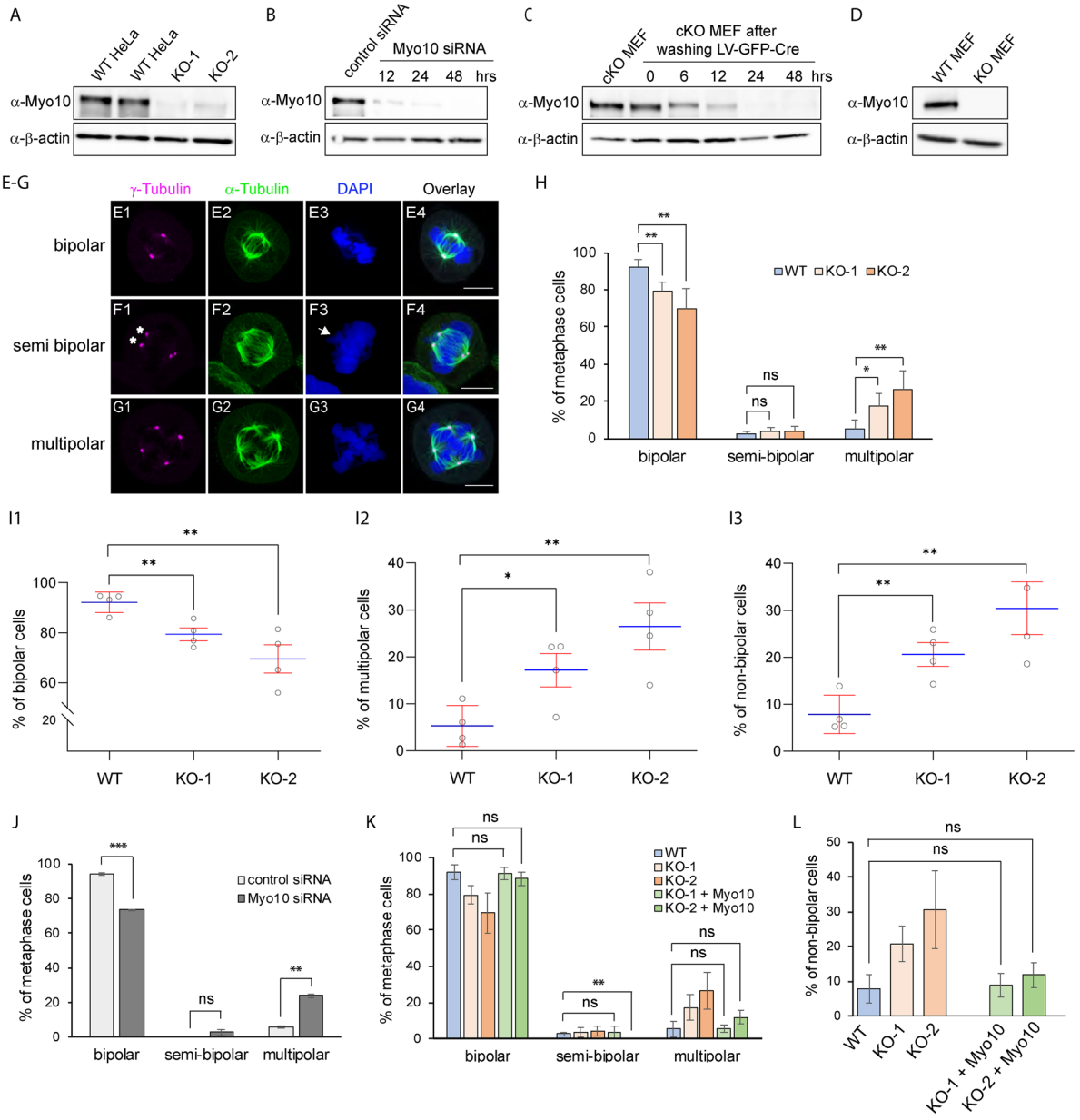

FIGURE 1: Metaphase Myo10 depleted cells exhibit a significant increase in the frequency of multipolar spindles. (A–D) Westerns blots of whole cell extracts prepared from WT, KO-1, and KO-2 HeLa cells (A), HeLa cells treated twice for 48 h each with a control, nontargeting siRNA or a Myo10 Smartpool siRNA, and collected 12, 24, and 48 h after starting the second treatment (B), nontransduced cKO MEFs and cKO MEFs 0, 6, 12, 24, and 48 h after transduction with lentiviral cre (C), and MEFs from a WT B6 mouse and from the tm1d Myo10 KO mouse (D), all probed for Myo10 and β-actin as a loading control. (E1–E4) A metaphase HeLa cell harboring a bipolar spindle that was stained for γ-tubulin, α-tubulin, and DNA (DAPI), along with the overlay (see Z-Stack Movie 1). (F1–F4) Same as E1–E4 except that this HeLa cell harbored a semibipolar spindle (see Z-Stack Movie 2). The two γ-tubulin-positive poles with asterisks indicate they were in different z planes, resulting in chromosome distortion (arrow in F3). (G1–G4) Same as E1–E4 except that this HeLa cell harbored a multipolar spindle (see Z-Stack Movie 3). (H) Quantitation at metaphase of the percent of bipolar, semibipolar, and multipolar spindles in WT HeLa (281 cells), KO-1 (289 cells), and KO-2 (307 cells) from four experiments. (I1–I3) Comparison of WT Hela with KO-1 and KO-2 with regard to percent bipolar cells (I1), percent multipolar cells (I2) and percent nonbipolar cells (semibipolar plus multipolar), all at metaphase (calculated from the raw data in (H); shown as SEMs). (J) Quantitation at metaphase of the percent of bipolar, semibipolar, and multipolar spindles in HeLa cells treated twice with either a control, nontargeting siRNA or Myo10 Smartpool siRNA (173 control cells and 234 KD cells from two experiments). (K) Quantitation at metaphase of the percent of bipolar, semibipolar, and multipolar spindles in WT HeLa, KO-1, and KO-2, and in KO-1 and KO-2 24 h posttransfection with mScarlet-Myo10 (103 KO-1 cells and 120 KO-2 cells from four experiments; only cells expressing mScarlet-Myo10 were scored; only statistical values for WT vs. rescued KO-1 and KO-2 cells are shown; the values for WT HeLa, KO-1 and KO-2 are from (H)). (L) Quantitation at metaphase of the percent of nonbipolar spindles (semibipolar plus multipolar) in WT HeLa, KO-1, and KO-2, and in KO-1 and KO-2 24 h posttransfection with mScarlet-Myo10 (only statistical values for WT vs. rescued KO-1 and KO-2 cells are shown; the values for WT HeLa, KO-1, and KO-2 are from (H)). All mag bars are 10 μm.

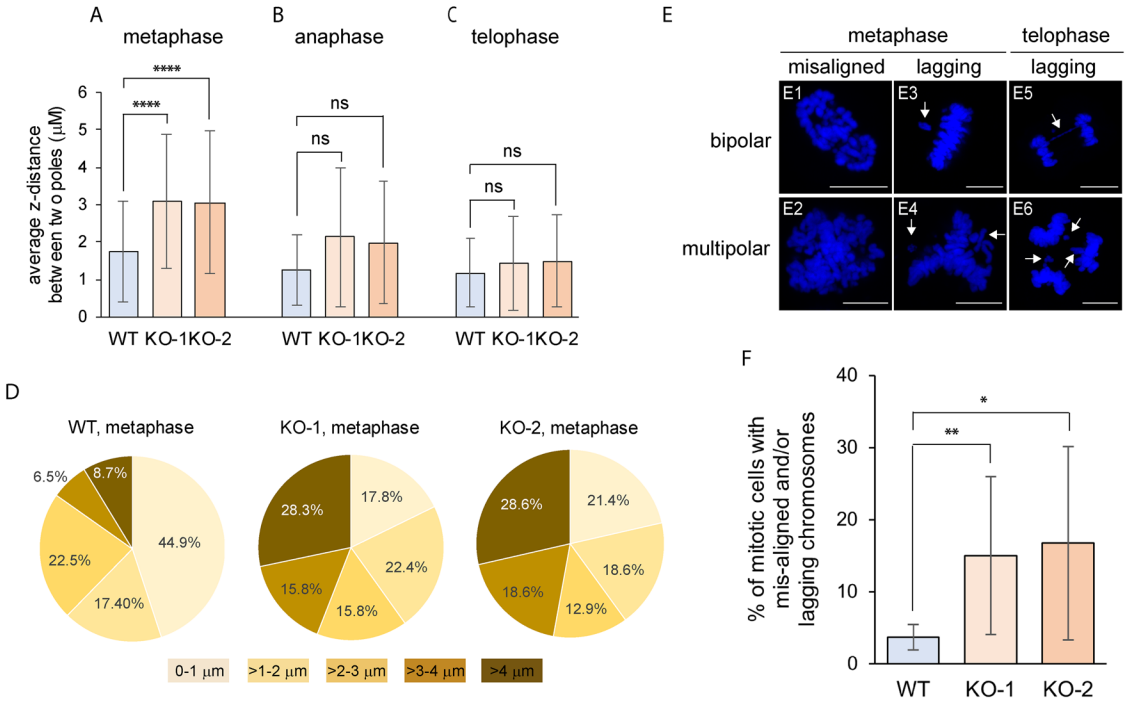

FIGURE 2: Metaphase Myo10 depleted cells exhibit increased frequencies of spindles that are not parallel to the substratum, misaligned chromosomes, and lagging chromosomes. (A–C) Average distance in Z between the two poles of bipolar WT HeLa, KO-1, and KO-2 at metaphase (A), anaphase (B) and telophase (C; 180 WT, 234 KO-1 and 228 KO-2 cells from four experiments; see Z-Stack Movies 4–6). (D) The distributions of the values in (A) in 1-μm intervals. (E1–E6) Shown are representative examples of misaligned chromosomes at metaphase in KO-1 cells undergoing bipolar mitosis (E1) or multipolar mitosis (E2), and lagging chromosomes at metaphase and telophase in KO-1 cells undergoing bipolar mitosis (E3 and E5, respectively) or multipolar mitosis (E4 and E6, respectively; arrows point to lagging chromosomes). (F) Percent of mitotic WT HeLa, KO-1 and KO-2 that possess misaligned and/or lagging chromosomes (258 WT, 308 KO-1 and 330 KO-2 cells from four experiments). All mag bars are 10 μm.

(at which point we started collecting data). This behavior suggests that these clonal isolates underwent some kind of genetic or epigenetic change after CRISPR-based genome editing that ameliorated to some extent the cellular defects responsible for their slow growth rate. Given this, and given that both of our KO clones are slight hypomorphs, we decided to examine HeLa cells in which Myo10 was transiently depleted using siRNA-mediated KD. Relative to cells receiving a control, nontargeting siRNA, cells receiving two rounds of treatment with Myo10 SmartPool siRNA exhibited near complete depletion of Myo10 48 h after the second round (Figure 1B; Supplemental Figure S1B). At 48 h posttransfection, unsynchronized, and metaphase cells were scored for spindle phenotype as described above. Consistent with KO-1 and KO-2 cells, Myo10 KD cells exhibited a 20.7% reduction in the frequency of bipolar spindles and a 4.1-fold increase in the frequency of multipolar spindles (Figure 1J). We conclude, therefore, that this core phenotype is replicated in HeLa cells where Myo10 is transiently depleted using RNAi.

MEFs isolated from a Myo10 conditional KO mouse and transduced with lenti-Cre phenocopy Myo10-depleted HeLa cells

We recently described the creation of a Myo10 conditional knockout (cKO) mouse (tm1c) and several phenotypes exhibited by this mouse following its cross with a global Cre-deleter strain (Heimsath *et al.*, 2017). To provide additional support for the results obtained using Myo10-depleted HeLa cells, we treated primary MEFs isolated from this Myo10 cKO mouse with lentivirus expressing GFP-tagged Cre recombinase. Western blots showed that Myo10 was essentially undetectable 24–48 h after lenti-cre transduction (Figure 1C; Supplemental Figure S1C). Given this, nontransduced cKO MEFs and cKO MEFs 48 h after transduction with lenti-Cre were scored for their metaphase spindle phenotype. As with Myo10 depleted HeLa cells, scoring showed that lenti-Cre-transduced cKO MEFs exhibit a 35.6% decrease in the frequency of bipolar spindles, a 4.7-fold increase in the frequency of semipolar spindles, a 2.9-fold increase in the frequency of multipolar spindles, and a 3.6-fold increase in the frequency of nonbipolar spindles (semipolar plus multipolar; Supplemental Figure S2A). Also, like Myo10-depleted HeLa cells, optical sectioning of metaphase cells exhibiting just two poles showed that the average distance separating the two spindle poles in Z was significantly greater in the lenti-Cre-transduced cKO MEFs than in the nontransduced cKO MEFs (Supplemental Figures S2, B and C shows the distributions of these distances in 1-μm intervals). Finally, like Myo10-depleted HeLa cells, the percentage of lenti-Cre-transduced cKO MEFs exhibiting chromosome misalignment and/or lagging chromosomes was 6.9-fold higher than for nontransduced cKO MEFs (Supplemental Figure S2D). We conclude, therefore, that cKO MEFs subjected to the conditional and rapid depletion of Myo10 largely phenocopy Myo10-depleted HeLa cells as regards increased spindle multipolarity, abnormal spindle orientation, and increased frequencies of chromosome misalignment/lagging chromosomes.

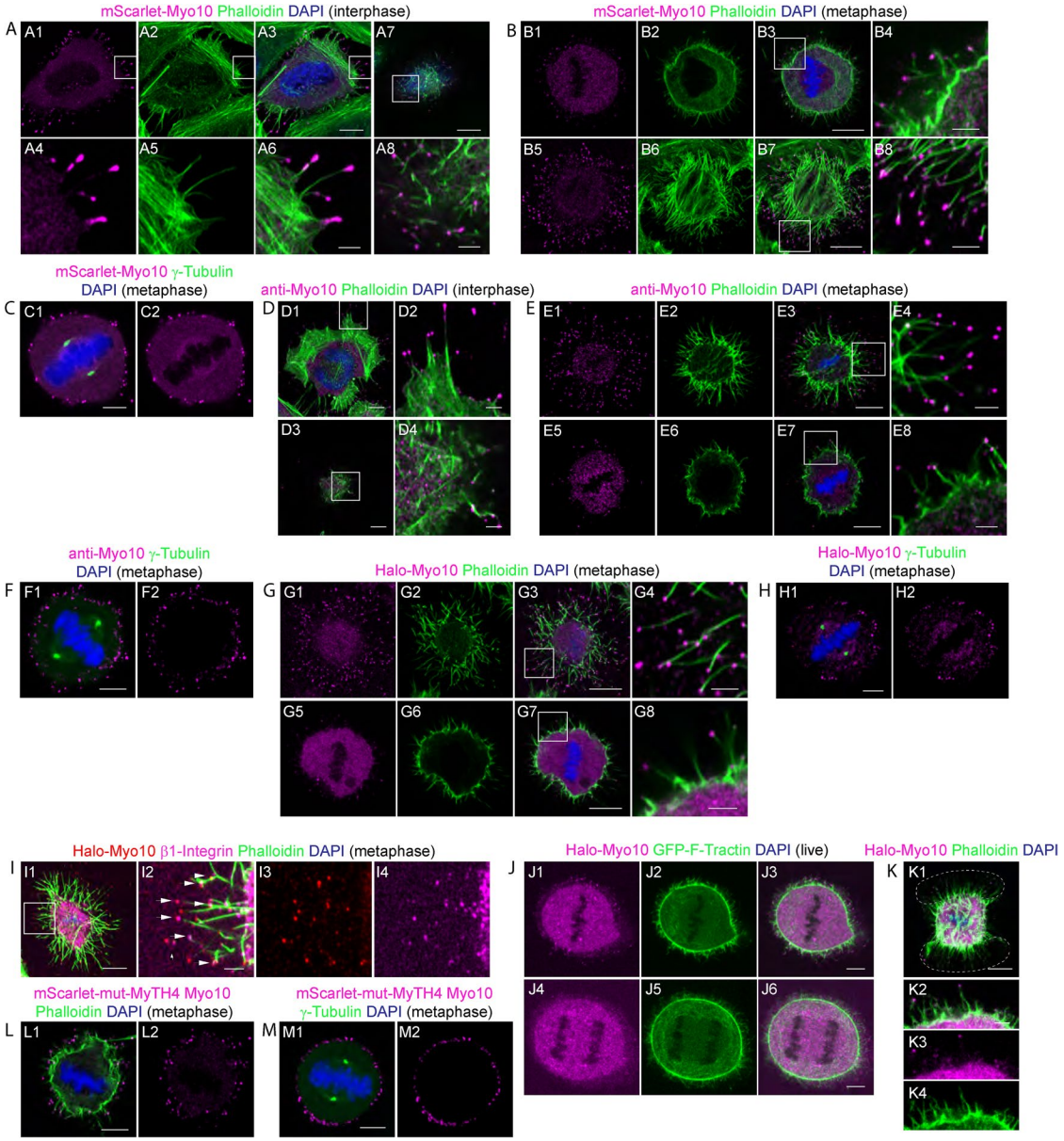

FIGURE 3: Myo10 localizes exclusively in metaphase cells to the spindle and to the tips of retraction fibers and dorsal filopodia. (A1–A6) An interphase Myo10 KO-1 cell expressing mScarlet-Myo10 stained with Alexa488-labeled Phalloidin and DAPI to show the accumulation of mScarlet-Myo10 at the tips of ventral filopodia. (A7 and A8) Same as in A1–A6 except an apical section to show the accumulation of mScarlet-Myo10 at the tips of dorsal filopodia. (B1–B4) A metaphase Myo10 KO-1 cell expressing mScarlet-Myo10 stained as in A1–A8 to show the dorsal, mScarlet-Myo10-positive filopodia at the cell's equator. (B5–B8) Same as B1–B4 except a ventral section to show the accumulation of mScarlet-Myo10 at the tips of retraction fibers (see Z-Stack Movie 7). (C1 and C2) A metaphase Myo10 KO-1 cell expressing mScarlet-Myo10 stained with anti-γ-tubulin-AF488 and DAPI (equatorial section; see Z-Stack Movie 8). (D1–D4) An interphase HeLa cell stained with anti-Myo10, Alexa488-labeled Phalloidin and DAPI to show the accumulation of endogenous Myo10 at the tips of ventral (D1 and D2) and dorsal (D3 and D4) filopodia. (E1–E4) A metaphase HeLa cell stained as in D1–D4 to show the accumulation of endogenous Myo10 at the tip's ventral retraction fibers. (E5–E8) Same as E1–E4 except an equatorial section to show the accumulation of endogenous Myo10 at the tips dorsal filopodia (see Z-Stack Movie 9). (F1 and F2) A metaphase HeLa cell stained with anti-Myo10, anti-γ-tubulin-AF488 and DAPI (equatorial section; see Z-Stack Movie 10). (G1–G4) A metaphase Halo–Myo10 KI cell stained with Alexa488-labeled Phalloidin and DAPI to show the accumulation of Halo–Myo10 at the tips of ventral filopodia. (G5–G8) Same as G1–G4 except an equatorial section to show the accumulation of endogenously tagged Myo10 at the tips dorsal filopodia (see also Z-Stack Movie 11). (H1 and H2) A metaphase Halo–Myo10 KI cell stained with anti-γ-tubulin-AF488 and DAPI (equatorial section; see Z-Stack Movie 12). (I1–I4) A metaphase Halo–Myo10 KI cell stained Alexa488-labeled Phalloidin, DAPI and an antibody to the open, active form of β1 integrin (ITGB1 9EG7), and imaged to show the signals for Myo10 and active integrin in ventral retraction fibers (arrowheads points sites of colocalization between Myo10 and active integrin). (J1–J3) Single frame from a time lapse movie of a metaphase Halo–Myo10 KI cell expressing GFP-F-Tractin (equatorial section). (J4–J6) Same as J1–J3 except at anaphase (see Movie 13). (K1) A Halo-Myo10 KI cell that was plated on an I bar

MEFs from the straight Myo10 KO mouse exhibit an increase in the frequency of multipolar spindles whose magnitude depends on embryo phenotype and culture density

We next characterized the mitotic phenotype of MEFs isolated from the straight Myo10 KO mouse (tm1d; created by crossing the cKO Myo10 KO mouse (tm1c) with a global cre deleter strain; Heimsath *et al.*, 2017). The fate of embryos in single litters from this mouse range from early embryonic lethality associated with exencephaly to viable mice exhibiting small body size, webbed digits, white belly spots, and microphthalmia. Given that the tm1d mouse is on a pure B6 background, this wide variation in embryo fate must be due to incomplete penetrance/variable expressivity rather than to variations between embryos in genetic modifiers (Dickinson *et al.*, 2016). We decided, therefore, to characterize MEFs isolated from both nonexencephalic and exencephalic tm1d embryos. We also decided to score their mitotic defects 24 h after seeding them densely (5×10^4 cells/cm^2), at moderate density (2.5×10^4 cells/cm^2), and sparsely (0.5×10^4 cells/cm^2). This decision was based on measurements of growth rates for cells seeded at these three densities (referred to below and in the figures as "dense or D", "moderate or M", and "sparse or S"), where the growth of WT MEFs was unaffected by seeding density, while the growth of both nonexencephalic and exencephalic KO MEFs was significantly slower at the sparse seeding density (Supplemental Figure S3A), as well as significantly slower than WT MEFs at the sparse seeding density (Supplemental Figure S3B). These results raised the possibility that Myo10 KO MEFs exhibit more mitotic defects when the spatial cues provided by neighboring cells are attenuated. Consistently, exencephalic KO MEFs exhibited higher frequencies of multipolar spindles as the cell density was lowered (Supplemental Figure S3C). Moreover, the frequencies for both KO MEFs were significantly higher than the frequency for WT MEFs at both moderate and sparse seeding densities (Supplemental Figure S3D). Additionally, the frequency exhibited by exencephalic KO MEFs was significantly higher than the frequency exhibited by nonexencephalic KO MEFs at both moderate and sparse seeding densities (Supplemental Figure S3D). Together, these results show that MEFs isolated from the straight Myo10 KO mouse exhibit a significant increase in the frequency of multipolar spindles, and that the severity of this defect depends on the phenotype of the embryo from which the MEFs are isolated and on the density at which they are cultured. Finally, both nonexencephalic and exencephalic KO MEFs grown at moderate density exhibit an increase in the frequency of spindles that are not parallel to the substrate (Supplemental Figure S3, E and F).

The multipolar phenotype exhibited by Myo10-depleted HeLa cells is rescued by reexpression of Myo10

The fact that the multipolar spindle phenotype exhibited by Myo10-depleted HeLa cells is also seen in Myo10 KD HeLa cells, cre-treated Myo10 cKO MEFs, and straight Myo10 KO MEFs argues that it is indeed a consequence of Myo10 depletion/loss. That said, we thought it was important to show that reintroducing Myo10 into Myo10-depleted HeLa cells can rescue the multipolar spindle phenotype before proceeding with efforts to define underlying mechanisms in these cells. Towards that end, we transfected KO-1 and KO-2 with mScarlet-Myo10 and scored expressing cells at metaphase for spindle phenotype. Statistical analyses showed that Myo10 reexpression restored the values for the percentage of metaphase cells with bipolar and multipolar spindles in both KO lines to WT levels (Figure 1K). Moreover, combining the data for semibipolar and multipolar spindles into nonpolar spindles showed that both KO lines were completely rescued (Figure 1L). Together, these results paved the way for defining underlying mechanisms by complementation.

Myo10 localizes exclusively in metaphase cells to the spindle and the tips of retraction fibers

We used KO-1 cells rescued with mScarlet-Myo10 to examine the localization of Myo10, focusing in part on its reported localization at spindle poles (Woolner *et al.*, 2008) and in subcortical actin clouds at the cell equator (Kwon *et al.*, 2015). As expected (Sousa and Cheney, 2005; Kerber and Cheney, 2011; Weck *et al.*, 2017; Tokuo, 2020), mScarlet-Myo10 localized robustly at the tips of both ventral (Figure 3, A1–A6) and dorsal filopodia (Figure 3, A7 and A8; apical plane) during interphase, and at the tips of dorsal filopodia during metaphase (Figure 3, B1–B4; equatorial plane). Also, as expected (Iwano *et al.*, 2015; Kwon *et al.*, 2015), mScarlet-Myo10 localized dramatically at the tips of metaphase retraction fibers (Figure 3, B5–B8). In contrast, Z-Stacks of 77 mScarlet-Myo10-expressing metaphase cells stained for DNA and F-actin showed no evidence that it localizes to spindle poles (Z-Stack Movie 7). Similarly, Z-Stacks of 166 out of 171 mScarlet-Myo10-expressing metaphase cells stained for DNA and y-tubulin showed no evidence that the expressed myosin localizes to spindle poles (Figure 3, C1 and C2; Z-Stack Movie 8). Finally, Z-Stacks of the 77 mScarlet-Myo10-expressing cells stained for DNA and F-actin, and the 171 mScarlet-Myo10-expressing cells stained for DNA and y-tubulin, showed no evidence that the expressed myosin is enriched in equatorial, subcortical zones during metaphase (Z-Stack Movies 7 and 8).

To seek additional support for these findings, some of which are at odds with previous reports, we examined Myo10 localization in WT HeLa cells by staining for endogenous Myo10 using a Myo10 antibody whose specificity we confirmed using Myo10 KO-1 (Supplemental Figure S4, A1–A5 and B1–B5). As expected, endogenous Myo10 localizes robustly at the tips of ventral and dorsal filopodia during interphase (Figure 3, D1–D4), and at the tips of retraction fibers (Figure 3, E1–E4) and dorsal filopodia (Figure 3, E5–E8; equatorial plane) during metaphase. In agreement with the results obtained using mScarlet-Myo10, Z-Stacks of 83 metaphase cells stained for Myo10, DNA and F-actin showed no evidence that

pattern of fibronectin (dashed white outline) and stained at metaphase with Alexa488-labeled Phalloidin and DAPI (shown is a ventral section to reveal the distribution of retraction fibers; see Z-Stack Movie 14). (K2–K4) Equatorial section of the cell in K1. (L1 and L2) A metaphase Myo10 KO-1 cell expressing mScarlet-mut-MyTH4 Myo10 stained with Alexa488-labeled Phalloidin and DAPI (equatorial section; see Z-Stack Movie 16). A metaphase Myo10 KO-1 cell expressing mScarlet-mut-MyTH4 Myo10 stained with anti-γ-tubulin-AF488 and DAPI (equatorial section; see Z-Stack Movie 17). Note that the bright dots in the Myo10 channel at the very perimeter of the metaphase cells stained for γ-tubulin in C, F, H, and M (equatorial sections) are mScarlet-Myo10 (C), endogenous Myo10 (F), Halo-Myo10 (H), and mScarlet-mut-MyTH4 Myo10 (M) at the tips of dorsal filopodia. The mag bars in A3, A7, B3, B7, D1, D3, E3, E7, G3, G7, I1, K1, L1, and M1 are 10 μm. The mag bars in C1, F1, H1, J3, and J6 are 5 μm. The mag bars in A6, A8, B4, B8, D2, D4, E4, E8, G4, G8, I2, and K2 are 2 μm. Of note, the faint, diffuse fluorescence seen throughout the cytoplasm in most cells likely corresponds to folded, freely-diffusing, cargo-free Myo10 (Umeki *et al.*, 2011; Baboolal *et al.*, 2016; Liu *et al.*, 2021).

endogenous Myo10 localizes to spindle poles (Z-Stack Movie 9). Consistently, Z-Stacks of 102 metaphase cells stained for Myo10, DNA and y-tubulin also showed no evidence of endogenous Myo10 at spindle poles (Figure 3, F1 and F2; Z-Stack Movie 10). Finally, Z-Stacks of the 83 cells stained for Myo10, DNA and F-actin, and the 102 cells stained for Myo10, DNA and y-tubulin, showed no evidence that endogenous Myo10 is enriched in equatorial, subcortical zones during metaphase (Z-Stack Movies 9 and 10).

Given that the localization of Myo10 at spindle poles and in subcortical actin clouds at the equator of dividing cells were central to previous models for how Myo10 stabilizes spindle poles (Woolner *et al.*, 2008) and facilitates the clustering of supernumerary centrosomes (Kwon *et al.*, 2015), respectively, we sought to confirm our localization data by endogenous tagging of Myo10 using CRISPR (see *Materials and Methods*). This effort resulted in the creation of a Halo-Myo10 KI HeLa cell line in which the Myo10 present in one allele is tagged at its N-terminus with Halo (Supplemental Figure S5A). As expected, Halo-Myo10 localizes robustly at the tips of filopodia in interphase cells (Supplemental Figure S5, B1 and B2) and at the tips of retraction fibers (Figure 3, G1–G4) and dorsal filopodia (Figure 3, G5–G8; equatorial plane) in metaphase cells. Consistent with the role that retraction fibers play in cell adhesion during mitosis, and with Myo10's ability to promote adhesion via its FERM domain-dependent interaction with β1-integrin, a significant fraction of Halo–Myo10 at the tips of retraction fibers colocalizes with the open, active form of β1-integrin (Figure 3, I1–I4; see arrowheads). Importantly, Z-Stacks of 72 metaphase KI cells stained for DNA and F-actin showed no evidence that Halo-Myo10 is enriched at spindle poles (Z-Stack Movie 11). Similarly, Z-Stacks of 107 metaphase KI cells stained for DNA and y-tubulin showed no evidence that Halo-Myo10 localizes to spindle poles (Figure 3, H1 and H2; Z-Stack Movie 12). Moreover, Z-Stacks of the 72 metaphase KI cells stained for DNA and F-actin, and the 107 metaphase KI cells stained for DNA and y-tubulin, showed no evidence that Halo–Myo10 is enriched in equatorial, subcortical zones during metaphase (Z-Stack Movies 11 and 12). Consistently, time lapse movies of Halo–Myo10 KI cells expressing the F-actin probe GFP-F-Tractin failed to detect an enrichment of Halo–Myo10 within subcortical areas at the equator of either metaphase (Figure 3, J1–J3) or anaphase cells (Figure 3, J4–J6; Movie 13). Regarding this localization, Kwon *et al.* (2015) argued that the Myo10 present there serves to connect the base of retraction fibers to the tips of astral microtubules via its MyTH4 domain to promote supernumerary centrosome clustering. To provide further support for this idea, they imaged cells dividing on an I bar pattern of fibronectin to restrict the attachment of retraction fibers to opposite sides of the cell cortex. In their images, overexpressed, GFP-tagged Myo10 was enriched within these two areas relative to the rest of the equatorial cortex. We repeated this experiment using our Halo–Myo10 KI cells and saw no such enrichment (Figure 3, K1–K4; Z-Stack Movie 14; representative of ~20 cells imaged). Enrichment was also not seen in KO-1 cells expressing mScarlet–Myo10 (Z-Stack Movie 15).

Finally, ~90% of mScarlet–Myo10 expressing cells, ~74% of immunostained cells, and ~86% of Halo–Myo10 KI cells exhibit a faint signal for Myo10 in the spindle (see, for example, Figure 3, C2, E5, and H2). To gauge the specificity of this faint signal, we imaged KO-1 cells rescued with mScarlet–Myo10 harboring a MyTH4 domain containing four closely spaced point mutations that abrogate microtubule interaction (see below for details). Importantly, only ~7% of metaphase cells expressing mScarlet-mut-MyTH4 Myo10 exhibited any signal in the spindle, and in each of these cases the signal was very faint (Figure 3, L1, L2, M1, and M2 show examples where no spindle signal was detectable; Z-Stack Movies 16 and 17; note that mut-MyTH4 Myo10 localizes normally to the tips of retraction fibers and dorsal filopodia). This result demonstrates that Myo10 only appears in the spindle when it is capable of interacting with microtubules. Given this, and given that the majority of transfected, immunostained and KI cells exhibit the Myo10 spindle signal, we conclude that this signal, while faint, is real, that is, that Myo10 localizes to the spindle (see also Weber *et al.*, 2004 and Woolner *et al.*, 2008).

In summary, all of our results agree on four aspects of Myo10 localization in metaphase HeLa cells. First, Myo10 is not present at spindle poles (of note, this may not be the case in other cells types; Woolner *et al.*, 2008; Pozo *et al.*, 2021). Second, Myo10 is not concentrated in subcortical areas at the equator of dividing cells. Third, Myo10 localizes to the spindle in a MyTH4 domain-dependent manner. Fourth, Myo10 localizes dramatically at the tips of retraction fibers and dorsal filopodia.

Multipolar spindles in Myo10-depleted HeLa cells arise from a combination of PCM fragmentation and an inability to cluster supernumerary centrosomes

We used our Myo10-depleted HeLa cells to search for the cause(s) of spindle multipolarity when Myo10 is missing. Four distinct cellular defects can give rise to multipolar spindles (reviewed in Maiato and Logarinho, 2014). Two of these defects, cytokinesis failure and centriole overduplication, give rise to multipolar spindles because they generate interphase cells with extra centrosomes. The third defect, centriole disengagement, gives rise to multipolar spindles because both separated centrioles can serve as microtubule organizing centers (MTOCs). Finally, PCM fragmentation gives rise to multipolar spindles because the acentriolar PCM fragments generated can serve as MTOCs. Consistent with the results of Kwon et al using Myo10 KD HeLa cells (Kwon *et al.*, 2015), we did not see a significant difference between WT and Myo10-depleted HeLa cells in the average number of nuclei per cell (Supplemental Figure S6, A1 and A2), arguing that cytokinesis failure does not contribute significantly to their multipolar spindle phenotype. Centriole overduplication also does not appear to be responsible, as unsynchronized WT and Myo10-depleted HeLa cells have the same number of centrioles (Supplemental Figure S6B). For normal cells, which possess one centrosome, that would leave centriole disengagement and PCM fragmentation as the remaining possible causes of spindle multipolarity. For cancer cells, which often possess supernumerary centrosomes, the inability to cluster the extra spindle poles that ensue represents another possible cause of spindle multipolarity (reviewed in Godinho *et al.*, 2009; Cosenza and Krämer, 2016; Rhys and Godinho, 2017). Given that a significant fraction of HeLa cells possesses supernumerary centrosomes (see below), and that Myo10 has been implicated in promoting the clustering of the extra poles that ensue (Kwon *et al.*, 2015), subsequent experiments were designed to distinguish between centriole disengagement, PCM fragmentation, and an inability to cluster extra poles in cells with supernumerary centrosomes as causes of spindle multipolarity.

To accomplish this, we stained Myo10-depleted HeLa cells for γ-tubulin and the centriole marker centrin-1 (along with DAPI), as this staining regimen reveals MTOCs arising from both acentriolar PCM fragments and centriole-containing structures. Imaging of unsynchronized, metaphase Myo10-depleted HeLa cells stained in this way revealed examples of multipolar spindles caused by all three mechanisms discussed above. For example, Z-Stack Movie 18, along with the enlarged images of this cell's three presumptive spindle poles (Figure 4A1), represents an example of spindle multipolarity driven by centriole disengagement (note that two of this cell's

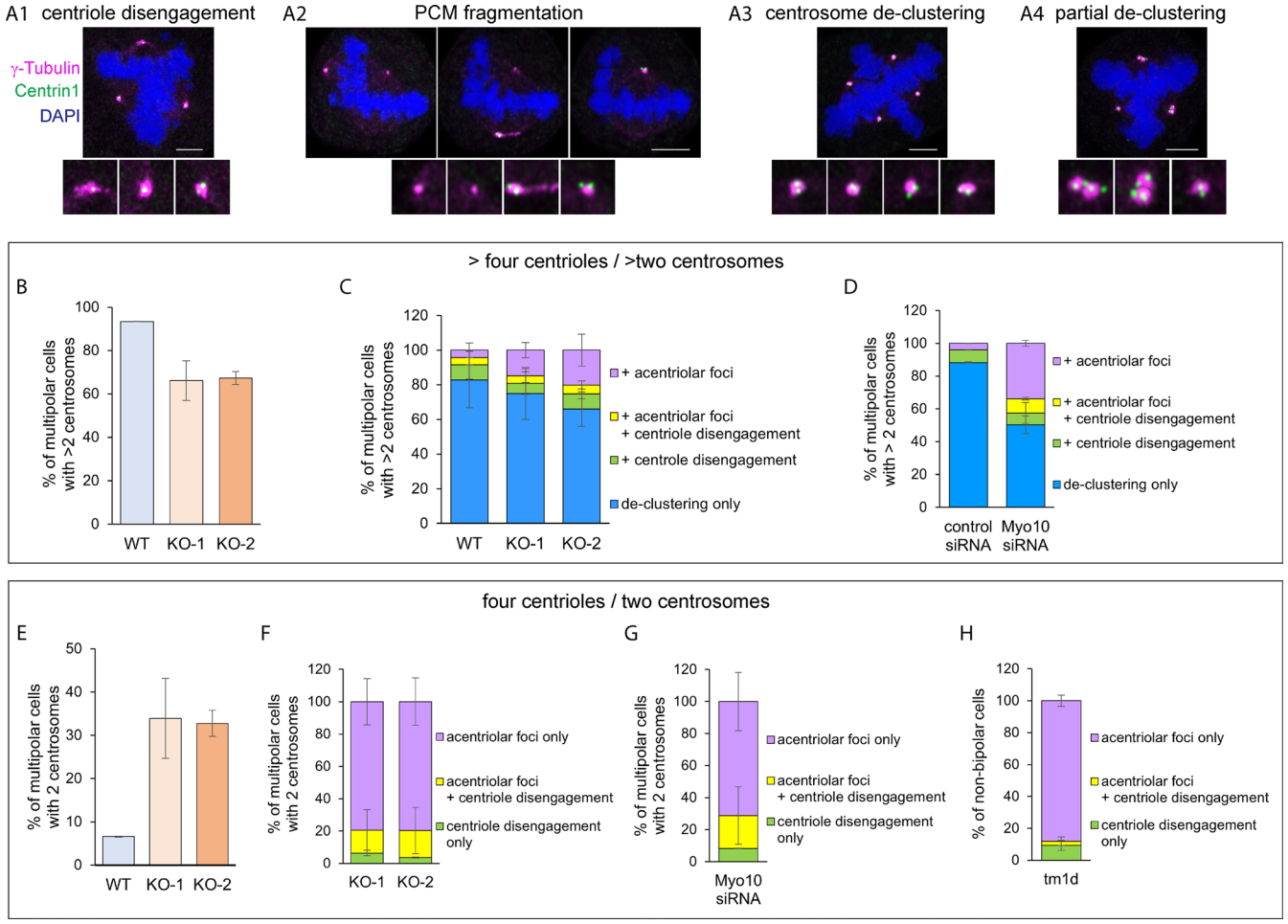

FIGURE 4: Causes of spindle multipolarity in Myo10-depleted HeLa cells and Myo10 KO MEFs. (A1–A4). Representative images of cells stained for γ-tubulin, centrin-1, and DNA that exhibit centriole disengagement (A1), PCM fragmentation (A2; shown are three different focal planes in one cell), centrosome declustering (A3), and partial centrosome declustering (A4). (B) Percent of multipolar WT HeLa, KO-1, and KO-2 that have more than four centrioles/two centrosomes. (C) Percent of multipolar WT HeLa, KO-1, and KO-2 with more than four centrioles/two centrosomes that exhibit centrosome declustering only (blue), centrosome declustering plus acentriolar foci (purple), centrosome declustering plus centriole disengagement (green), or centrosome declustering plus acentriolar foci and centriole disengagement (yellow). (D) Percent of multipolar HeLa cells exhibiting the mitotic defects described in Panel C that had been treated with control siRNA or Myo10 siRNA, and that had more than four centrioles/two centrosomes. (E) Percent of multipolar KO-1 and KO-2 with four centrioles/two centrosomes. (F) Percent of multipolar WT HeLa, KO-1, and KO-2 with four centrioles/two centrosomes that exhibit acentriolar foci (purple), acentriolar foci plus centriole disengagement (yellow), or centriole disengagement only (green). (G) Percent of multipolar HeLa cells exhibiting the mitotic defects described in Panel F that had been treated with Myo10 siRNA and that had four centrioles/two centrosomes (H) Percent of nonbipolar (semipolar plus multipolar) Myo10 KO MEFs isolated from the tm1d mouse that exhibit the mitotic defects described in Panel F. All mag bars are 5 μm.

three presumptive spindle poles possess only one centriole). Z-Stack Movie 19, along with the enlarged images of this cell's four presumptive spindle poles (Figure 4A2), represents an example of spindle multipolarity driven by PCM fragmentation (note that two of this cell's four presumptive spindle poles correspond to γ-tubulin-positive, acentriolar foci). More extreme examples of multipolar spindles driven by PCM fragmentation were also seen (Supplemental Figure S7A and Z-Stack Movie 20; Supplemental Figure S7B and Z-Stack Movie 21). Finally, the still images in Figure 4, Panel A3, show an example of spindle multipolarity driven by a failure to cluster the extra spindle poles that arise in cells with supernumerary centrosomes (i.e., referred to below as centrosome declustering; note that this cell contains four presumptive spindle poles, each possessing two centrioles). Examples of partial supernumerary centrosome declustering were also observed (Figure 4A4; note that only two of this cell's three presumptive spindle poles [the two with four centrioles] were created by supernumerary centrosome clustering).

To quantitate the relative contributions made by centriole disengagement, PCM fragmentation, and centrosome declustering to the multipolar spindle phenotype, we divided WT and Myo10-depleted HeLa cells exhibiting multipolar spindles into two groups: those with more than two normal centrosomes/poles each possessing two centrioles (i.e., ">four centrioles/>two centrosomes", where extra spindle poles can come from defects in supernumerary centrosome clustering, centriole disengagement, and/or PCM fragmentation), and those with two normal centrosomes/poles each possessing two centrioles (i.e., "four centrioles/two centrosomes", where extra spindle poles can only come from defects in centriole disengagement and/

or PCM fragmentation). For WT Hela, the vast majority of cells with multipolar spindles (93.4 ± 0.1%) contained more than four centrioles (Figure 4B). In 82.9 ± 16.3% of these cells, every γ-tubulin spot contained at least two centrioles (Figure 4C; WT blue), indicating that centrosome declustering was solely responsible for their multipolar spindle phenotype. For the remaining 17.1% of multipolar WT HeLa with more than four centrioles, 8.5 ± 8.0% exhibited centrosome declustering plus centriole disengagement (one or more γ-tubulin spots containing only one centriole; Figure 4C; WT green), 4.3 ± 4.0% exhibited centrosome declustering plus acentriolar foci (one or more γ-tubulin spots containing no centrioles; Figure 4C; WT purple), and 4.3 ± 4.0% exhibited centrosome declustering plus both centriole disengagement and acentriolar foci (Figure 4C; WT yellow).

For KO-1 and KO-2 cells, about two thirds of cells with multipolar spindles contained more than four centrioles (66.1 ± 9.2% for KO-1 and 67.3 ± 3.0% for KO-2; Figure 4B). In roughly two-thirds of these cells, every γ-tubulin spot contained at least two centrioles (74.9 ± 15.0% for KO-1 and 65.9 ± 9.9% for KO-2; Figure 4C; KO-1 blue, and KO-2 blue), indicating that centrosome declustering was mainly responsible for their multipolar spindle phenotype. Like WT HeLa, the remaining one-third of multipolar Myo10-depleted cells with more than four centrioles exhibited centrosome declustering plus either centriole disengagement, acentriolar foci, or both (Figure 4C; green, purple and yellow, respectively, for KO-1 and KO-2), although the percent of KO-1 cells and KO-2 cells exhibiting acentriolar foci was 3.4-fold and 4.7-fold higher than in WT HeLa cells, respectively (Figure 4C; compare the purple in KO-1 and KO-2 to the purple in WT). These results were supported by scoring those WT HeLa cells treated with Myo10 siRNA that contained more than four centrioles, which exhibited an 8.7-fold increase in the percentage of cells with acentriolar foci compared with HeLa cells treated with a control siRNA (Figure 4D; compare the purple in Myo10 siRNA to the purple in control siRNA).

Finally, and most interestingly, were the results for cells exhibiting multipolar spindles that contained only four centrioles (i.e., cells that did not possess supernumerary centrosomes), which corresponded to about one-third of Myo10-depleted cells (33.9 ± 9.2% for KO-1 and 32.7 ± 3.0% for KO-2) but only a tiny fraction of WT HeLa cells (6.6 ± 0.1%; Figure 4E). Importantly, acentriolar foci arising from PCM fragmentation was by itself responsible for about ~80% of the multipolar phenotype exhibited by this group of Myo10-depleted cells (79.4 ± 14.3% for KO-1 and 79.6 ± 14.7% for KO-2; Figure 4F; purple in KO-1 and KO-2). Of the remaining ~20% of multipolar Myo10-depleted cells with four centrioles, about three quarters exhibited acentriolar foci along with centriole disengagement (Figure 4F; yellow in KO-1 and KO-2). In total, therefore, 93.6% of multipolar KO-1 cells lacking supernumerary centrosomes, and 96.4% of KO-2 cells lacking supernumerary centrosomes, exhibited acentriolar foci, arguing that PCM fragmentation is the primary cause of spindle multipolarity in these cells. Importantly, very similar results were obtained for HeLa cells subjected to transient Myo10 depletion using Myo10 siRNA. Specifically, 91.9% of multipolar Myo10 KD cells that did not possess supernumerary centrosomes exhibited acentriolar foci arising from PCM fragmentation (Figure 4G; purple plus yellow in Myo10 siRNA). Together, these results argue that Myo10 supports spindle bipolarity in HeLa cells by promoting both PCM integrity and the clustering of supernumerary centrosomes.

Multipolar spindles in Myo10 KO MEFs arise primarily from PCM fragmentation

Staining of MEFs isolated from the straight Myo10 KO mouse, essentially all of which possessed only four centrioles/two centrosomes at metaphase, showed that acentriolar foci alone were responsible for 88% of the multipolar spindles observed (Figure 4H; purple). Of the remaining 12%, about one-third exhibited acentriolar foci plus centriole disengagement (Figure 4H; yellow). In total, therefore, ~92% of multipolar KO MEFs lacking supernumerary centrosomes exhibited acentriolar foci, arguing that PCM fragmentation is the primary cause of spindle multipolarity in these cells.

Acentriolar foci arising from PCM fragmentation serve as MTOCs during mitosis

The preceding analyses of multipolar cells were done using cells stained for DNA (DAPI), centrioles (centrin-1) and γ-tubulin, where presumptive spindle poles were identified based on DNA organization and staining for γ-tubulin. To provide additional evidence that PCM fragments lacking centrioles serve as spindle poles, we transfected KO-1 with dTomato-centrin-1 to mark centrioles, H2B-iRFP670 to mark chromatin, and EB1-EGFP to identify all MTOCs (i.e., those with centrioles and those lacking centrioles because they were created by PCM fragmentation). As expected, KO-1 cells containing two centriolar poles and undergoing normal bipolar mitoses exhibited EB1-EGFP comets emanating from two centriolar spindle poles (Supplemental Figure S8, A1 and A2; Z-Stack Movie 22). Also, as expected, KO-1 cells containing three centriolar poles and undergoing multipolar mitoses exhibited EBI-EGFP comets emanating from three centriolar spindle poles (Supplemental Figure S8, B1 and B2; Z-Stack Movie 23). Importantly, imaging EBI-EGFP in KO-1 cells undergoing multipolar mitoses also revealed microtubule asters emanating from acentriolar poles in addition to centriolar poles (Supplemental Figure S8, C1 and C2; Z-Stack Movie 24; enlarged images of centriolar and acentriolar spindle poles are shown in Movies 25 and 26, respectively). Together, these results confirm that PCM fragmentation creates acentriolar spindle poles that contribute to the multipolar phenotype exhibited by Myo10-depleted cells.

PCM/pole fragmentation occurs primarily at metaphase, arguing that it is a force-dependent event

Defects in spindle pole integrity that result in PCM/pole fragmentation commonly occur around metaphase when the chromosomal and spindle forces placed on the pole increase (Maiato and Logarinho, 2014). To determine when the PCM fragments in Myo10-depleted cells, we stained unsynchronized cells for γ-tubulin, centrin-1 and DAPI. Scoring the percent of cells containing only two centrosomes that exhibited y-tubulin-positive, centriole-negative PCM fragments showed that these acentriolar fragments only begin to appear at prometaphase and peak in frequency at metaphase (Figure 5A). Consistently, time lapse imaging of KO-1 cells expressing dTomato-centrin-1, H2B-iRFP670, and EB1-EGFP revealed PCM/pole fragmentation and the formation acentriolar poles as the cells approach metaphase (Movie 27). Time lapse imaging also showed that PCM/pole fragmentation results in rearrangements of chromosomes that can lead to defects in chromosome segregation (Movie 27). Together, these results indicate that cells do not enter mitosis with acentriolar PCM fragments, that PCM/pole fragmentation occurs primarily between prometaphase and metaphase, consistent with it being a force-dependent event, and that PCM/pole fragmentation can result in defects in chromosome segregation.

PCM fragmentation is not due to a defect in the pole localization of TPX2

Woolner and colleagues (2008) showed previously that frog epithelial cells depleted of Myo10 using morpholinos exhibit spindle pole

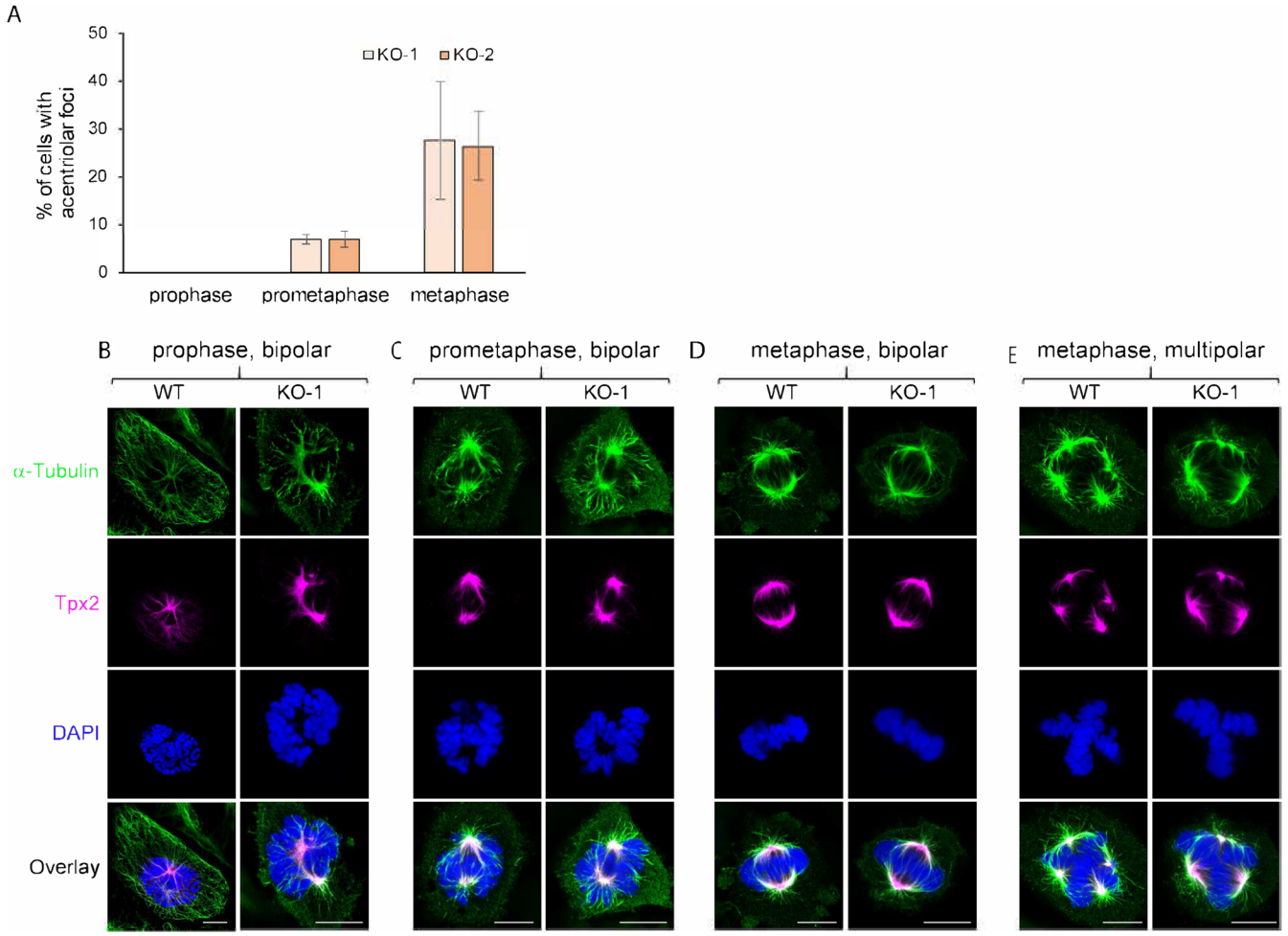

FIGURE 5: PCM/pole fragmentation is a force-dependent event that is not associated with a defect in TPX2 localization. (A) Shown is the percent of unsynchronized KO-1 and KO-2 cells containing only two centrosomes that exhibited y-tubulin-positive, centriole-negative PCM fragments at prophase, prometaphase and metaphase. (B–E) Representative images of WT and KO-1 cells at prophase (B), prometaphase (C), and metaphase (D and E) that were stained for α-tubulin, TPX2 and DNA (plus overlay) while undergoing bipolar divisions (B–D) or a multipolar division (E). All the mag bars are 10 μm.

fragmentation at metaphase, leading to an increase in the frequency of multipolar spindles. Importantly, they attributed this apparent defect in pole integrity to a defect in the localization of the spindle pole assembly factor TPX2 at and near poles. To determine whether the PCM fragmentation observed here is also associated with a defect in TPX2 localization, we stained WT and KO-1 for α-tubulin, TPX2 and DNA at prophase, prometaphase and metaphase. Figure 5, Panels B–D, show that Myo10-depleted cells undergoing bipolar mitosis do not exhibit any obvious defect in the localization of TPX2 at and near spindle poles at all three mitotic stages. Similarly, the localizations of TPX2 in WT and Myo10-depleted HeLa cells undergoing multipolar mitosis are indistinguishable (Figure 5E). These results indicate that the PCM fragmentation we observed here cannot be attributed to a defect in TPX recruitment to poles.

PCM fragmentation is likely not due to a general defect in spindle pole maturation

Defective spindle pole maturation can lead to defects in pole integrity that result in pole fragmentation (Maiato and Logarinho, 2014). To look for a defect in spindle pole maturation, we stained WT, KO-1, and KO-2 HeLa cells at prophase, prometaphase and metaphase for centrin-1, DNA, and the pole protein CDK5Rap2, which is known to accrue in maturing poles where it recruits γ-TuRC to promote microtubule nucleation (Varadarajan and Rusan, 2018; Vasquez-Limeta and Loncarek, 2021). Stained cells possessing only two poles were optically sectioned in 0.25-μm intervals and the total intensity of the CDK5Rap2 signal at poles obtained by summing slices. Representative images of stained poles in KO-1 cells are shown on Figure 6, Panels A–C. Importantly, quantitation revealed no significant differences between WT and KO-1 cells in the pole content of CDK5Rap2 at all three mitotic phases (Figure 6D). This result argues that PCM fragmentation is most likely not due to a general defect in pole maturation.

Myo10 must interact with both integrins and microtubules to promote spindle pole integrity but only needs interact with integrins to promote supernumerary centrosome clustering

We used complementation of Myo10-depleted HeLa cells to access the contributions made by the myosin's integrin-binding FERM domain and microtubule-binding MyTH4 domain to its ability to promote PCM/pole stability and supernumerary centrosome clustering.

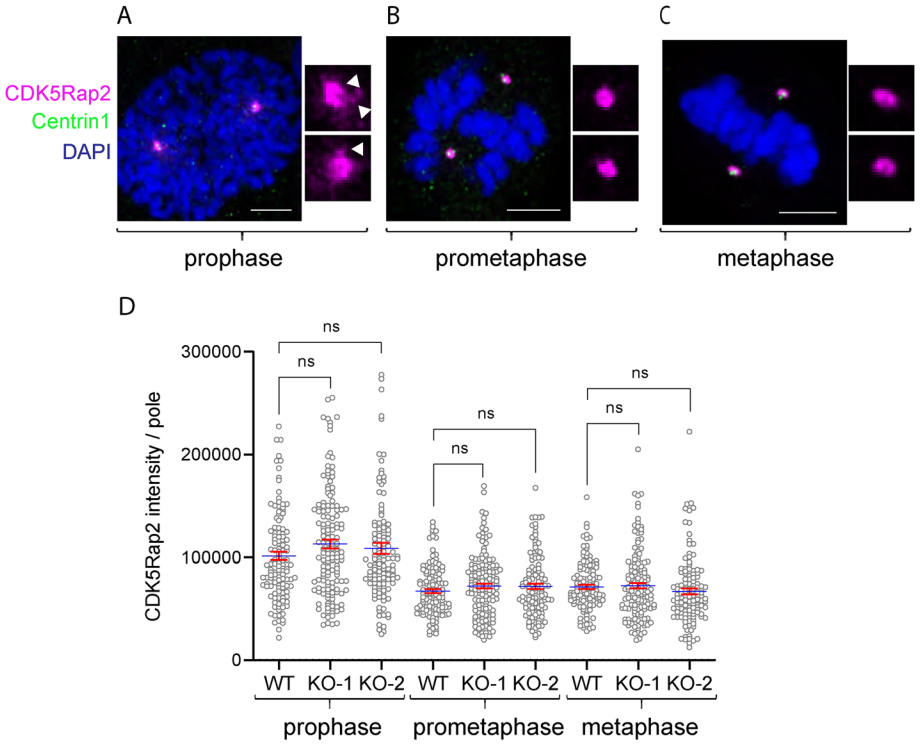

FIGURE 6: The defect in PCM/pole integrity is not due to an obvious defect in spindle pole maturation. (A–C) Representative images of unsynchronized KO-1 cells stained at prophase (A), prometaphase (B), and metaphase (C) for centrin-1, DNA, and the pole protein CDK5Rap2. The enlarged insets show the signal for CDK5Rap2 only (the white arrowheads in the insets for (A) point to CDK5Rap2-postive pericentriolar satellites). (D) Quantitation of the amount of CDK5Rap2 at poles in WT HeLa, KO-1, and KO-2 at prophase, prometaphase and metaphase (125 to 150 cells per condition from three independent experiments). The fact that the pole content of CDK5Rap2 is higher at prophase than at prometaphase and metaphase may be due to the presence of CDK5Rap2-positive pericentriolar satellites surrounding the poles at prophase but not at prometaphase and metaphase. All mag bars are 5 μm.

To accomplish this, we introduced function blocking point mutations within these two domains in the context of full length, mScarlet tagged Myo10 (see *Materials and Methods*; Supplemental Figure S9 for details). WT Myo10 and these two mutated versions of Myo10 (referred to as mut-FERM Myo10 and mut-MyTH4 Myo10) were expressed in KO-1 cells by creating stable, Tet-inducible lines. As anticipated, doxycycline addition resulted in the expression of all three proteins with the correct molecular weight for tagged, full length Myo10 (Figure 7A) and at a level that slightly exceeded that of endogenous Myo10 (WT Myo10, mut-FERM Myo10 and mut-MyTH4 Myo10 were expressed at about 2.2, 1.6, and 2.1 times the level of endogenous Myo10, respectively). Moreover, like WT Myo10 (Figure 3; Supplemental Figure S10, A1–A3 and D1–D4), both Myo10 mutants localize at the tips of interphase filopodia (Supplemental Figure S10, B1–B3 and C1–C3) and metaphase retraction fibers (Supplemental Figure S10, E1–E4 and F1–F4). Given these observations, an inability to rescue, whether partial or complete, cannot be attributed to lack of expression, significant variation in expression level between rescue constructs, or miss-localization of the mutant proteins.

As expected, WT Myo10 fully rescued the multipolar phenotype of KO-1 cells (Figure 7B). To estimate the contribution that its FERM and MyTH4 domains make to the clustering of extra spindle poles, we divided the number of rescued cells possessing more than four centrioles and a bipolar spindle by the total number of rescued cells with more than four centrioles (which encompass bipolar, semipolar, and multipolar cells) to obtain a value for the efficiency of supernumerary centrosome clustering. While cells rescued with WT Myo10 yielded a value of 72 ± 4.4%, cells rescued with mut-FERM Myo10 yielded a value of 11 ± 4.8% (Figure 7C). This result indicates that Myo10's ability to interact with integrins is essential for its ability to promote supernumerary centrosome clustering. In contrast, cells rescued with mut-MyTH4 Myo10 yielded a value of 62 ± 3.4%, indicating that Myo10's ability to interact with microtubules plays only a minor role in its ability to promote supernumerary centrosome clustering (Figure 7C).

To estimate the contribution that each domain makes to the maintenance of PCM/pole stability, we determined the underlying cause of multipolarity in rescued cells possessing only four centrioles. This was a minute fraction of cells rescued with WT Myo10 but about half of the cells rescued with mut-FERM Myo10 or mut-MyTH4 Myo10 (Figure 7D). For these latter two groups, multipolarity was associated almost entirely with PCM fragmentation, as indicated by the presence of acentriolar foci only (Figure 7E). This result argues that Myo10's FERM domain-dependent interaction with integrin and its MyTH4 domain-dependent interaction with microtubules are both required for its ability to promote PCM/pole integrity. The model in Figure 8 summarizes our conclusions regarding the mechanisms by which Myo10 supports spindle bipolarity.

DISCUSSION

Here we showed that the primary driver of spindle multipolarity exhibited by Myo10 KO MEFs and by Myo10-depleted HeLa cells lacking supernumerary centrosomes is PCM fragmentation, which creates γ-tubulin-positive, centriole-negative microtubule asters that serve as extra spindle poles. We also showed that the primary driver of spindle multipolarity in Myo10-depleted HeLa cells possessing supernumerary centrosomes is an inability to cluster the extra spindle poles that ensue. While our results are confirmatory with regard to Myo10 playing a role in spindle pole integrity and supernumerary centrosome clustering, our use of new tools has led us to new conclusions regarding the mechanisms by which Myo10 supports these two functions.

Extra spindle poles are created in the absence of centrosome amplification either through centriole disengagement or PCM fragmentation (reviewed in Maiato and Logarinho, 2014). Here we showed that the extra spindle poles in Myo10-depleted cells lacking supernumerary centrosomes are created almost entirely by PCM fragmentation. We also showed that PCM fragmentation occurs as cells approach metaphase, arguing that it is a force-dependent event. While force-dependent PCM fragmentation can happen when poles are structurally compromised in some way, we presented evidence that poles mature normally in Myo10-depleted cells. We also showed that Myo10 is not present at spindle poles, arguing against it having a direct role in maintaining pole stability

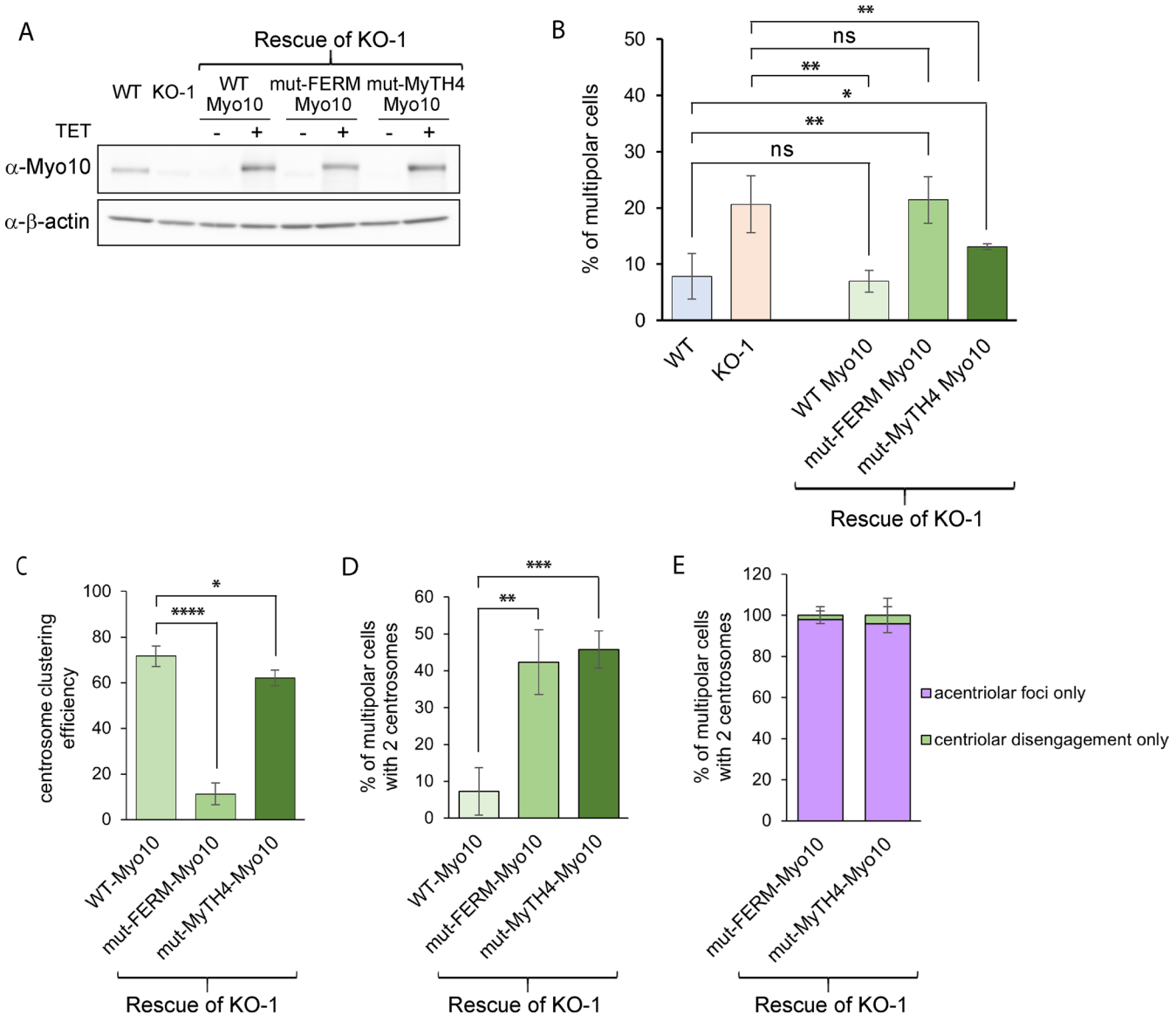

FIGURE 7: Complementation experiments reveal the contributions made by Myo10's FERM and MyTH4 domains to spindle pole integrity and supernumerary centrosome clustering. (A) Westerns blots of whole cell extracts prepared from WT HeLa, KO-1, and KO-1 rescued with mScarlet tagged WT Myo10, mut-FERM Myo10 or mut-MyTH4 Myo10 plus/minus doxycycline addition, and probed for Myo10 and for β-actin as a loading control. (B) Quantitation at metaphase of the percent of multipolar spindles in WT HeLa, KO-1, and KO-1 rescued with WT Myo10 (338 cells), mut-FERM Myo10 (386 cells) or mut-MyTH4 Myo10 (335 cells) (from three experiments). (C) The efficiency of supernumerary centrosome clustering in KO-1 rescued with WT Myo10 (76 cells), mut-FERM Myo10 (69 cells) or mut-MyTH4 Myo10 (75 cells; from three experiments). (D) The percent of multipolar cells with two centrosomes in KO-1 rescued with WT Myo10 (24 cells), mut-FERM Myo10 (44 cells), or mut-MyTH4 Myo10 (45 cells; from three experiments). (E) The percent of multipolar KO-1 cells with two centrosomes rescued with mut-FERM Myo10 or mut-MyTH4 Myo10 that exhibited acentriolar foci only or centriolar disengagement only (from three experiments).

(although see Woolner *et al.*, 2008 and Pozo *et al.*, 2021). What then is the reason why the PCM fragments when Myo10 is depleted? One important clue is our finding that Myo10 localizes to the spindle. While the spindle signal is relatively faint, our demonstration that it is not present in cells expressing a version of Myo10 that cannot bind to microtubules argues that it is real. We suggest that spindle microtubule-associated Myo10, presumably together with spindle-associated F-actin (Kita *et al.*, 2019), serves to maintain a balance in the forces exerted on poles, loss of which leads to PCM fragmentation. Of note, this mechanism would explain the MyTH4 domain requirement for pole stability demonstrated by complementation. It might also explain the FERM domain requirement whether proper adhesion also serves to maintain a balance in the forces exerted on poles (see Figure 8).

While our data indicated that PCM fragmentation contributes significantly to the formation of multipolar spindles in Myo10-depleted HeLa cells possessing supernumerary centrosomes, it indicated that the primary cause of spindle multipolarity in these cells is an inability to cluster their extra spindle poles. This result confirms and extends the observations made by Kwon *et al.* (2008) using RNAi screens for genes whose expression promotes supernumerary centrosome clustering, which implicated Myo10 in

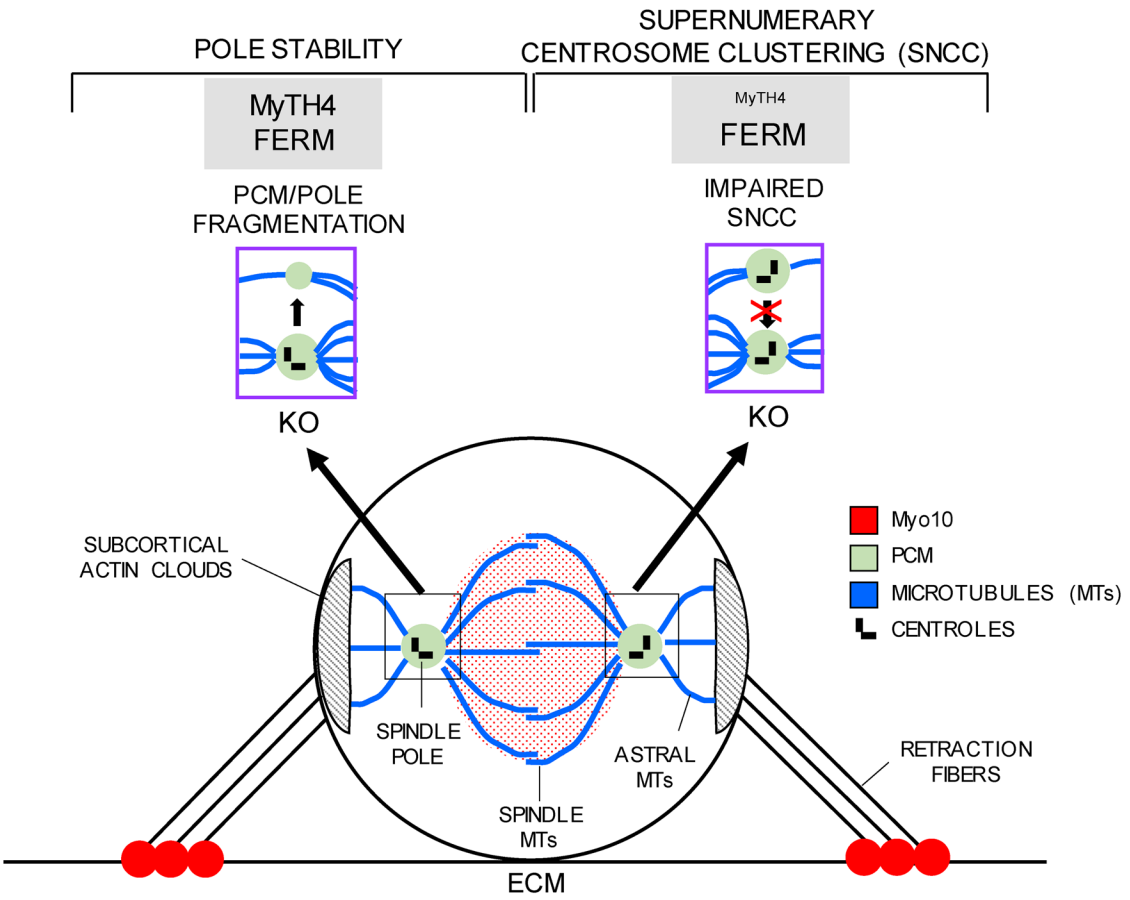

FIGURE 8: Mechanisms underlying Myo10's contribution to the maintenance of mitotic spindle bipolarity. Myo10 depleted cells exhibit two defects that lead to spindle multipolarity: PCM fragmentation (left) and impaired clustering of supernumerary centrosomes (right). PCM fragmentation creates y-tubulin-positive acentriolar foci that serve as extra spindle poles (left purple box), and is the major cause of spindle multipolarity in Myo10 KO MEFs. Impaired supernumerary centrosome clustering also results in extra spindle poles (right purple box) and is the major cause of spindle multipolarity in Myo10-depleted HeLa cells. Imaging of Halo-Myo10 KI cells shows that the myosin localizes exclusively during metaphase to the spindle and the tips of adhesive retraction fibers. The spindle signal, while faint, appears real as it lost when Myo10's microtubule-binding MyTH4 domain is mutated. Complementation shows that Myo10 must interact with both microtubules and integrins to promote PCM/pole integrity (upper left, shaded gray), arguing that Myo10 accomplishes this task at least in part by interacting with spindle microtubules. We suggest that spindle microtubule-associated Myo10, presumably together with spindle-associated F-actin (Kita *et al.*, 2019), serves to maintain a balance in the forces exerted on poles, loss of which leads to PCM fragmentation. For supernumerary centrosome clustering, complementation shows that Myo10 only needs interact with integrins via its FERM domain to support robust clustering (the MyTH4 domain makes only a minor contribution; upper right, shaded gray). These and other results argue that Myo10 promotes supernumerary centrosome clustering by supporting retraction fiber-based cell adhesion, which likely serves to anchor the microtubule-based forces driving pole focusing.

MDA-MB-231 cancer cells and fly Myo10A (a homologue of the human MyTH4/FERM myosin, Myo15) in near-tetraploid *Drosophila* S2 cells. Importantly, this screen also identified the pole focusing, microtubule minus end-directed kinesin 14 family member HSET (Ncd in *Drosophila*) as being essential for supernumerary centrosome clustering. In subsequent work, Kwon *et al.* (2015) showed that Myo10 with a mutated MyTH4 domain cannot rescue the defect in supernumerary centrosome clustering exhibited by Myo10 KD cells overexpressing PLK4. Given this, and given their evidence that Myo10 present within subcortical actin clouds at the equator of dividing cells cooperates in a MyTH4 domain-dependent manner with dynein to position the metaphase spindle, they proposed that this same pool of Myo10 cooperates in a MyTH4 domain-dependent manner with HSET to drive the clustering of supernumerary centrosomes.

We presented data here, on the other hand, that supports a FERM domain/adhesion-centric mechanism for how Myo10 promotes supernumerary centrosome clustering in HeLa cells. First, we confirmed that Myo10 localizes dramatically at the tips of retraction fibers. These actin-based structures are essential for the integrin-dependent adhesion of cells undergoing mitosis in two-dimension (Mitchison, 1992; Cramer and Mitchison, 1993, 1995, 1997; Dix *et al.*, 2018; Taubenberger *et al.*, 2020). Consistently, the signals for Myo10 and open, active integrin were seen to overlap significantly at retraction fiber tips. Second, we showed that the spindle in Myo10 depleted cells is often not parallel to the substratum. This result, and a similar result reported by Toyoshima and Nishida (2007) in Myo10 KD HeLa cells, is consistent with Myo10 depletion causing a defect in cell adhesion during mitosis. Third, and most importantly, our complementation experiments showed that Myo10's

ability to interact with integrins via its FERM domain is essential for its ability to promote supernumerary centrosome clustering. We note that all of these results are in line with the fact that Myo10 supports the formation of adhesions within filopodia and lamellipodia during interphase by virtue of its FERM domain-dependent interaction with β1-integrin (Zhang *et al.*, 2004; Hirano *et al.*, 2011; He *et al.*, 2017; Miihkinen *et al.*, 2021). They are also in line with micropatterning data showing that the ability of cancer cells to cluster supernumerary centrosomes is influenced significantly by the pattern of adhesion (Kwon *et al.*, 2008). What our results are not in line with, however, is the model proposed by Kwon *et al.* (2015) where Myo10 present in subcortical actin clouds at the cell equator drives supernumerary centrosome clustering in a MyTH4-domain-dependent manner. First, none of our localization approaches, including imaging of Halo–Myo10 KI cells, showed that Myo10 is concentrated in subcortical actin clouds. We suggest that Myo10 overexpression, combined with the collapse of Myo10-positive dorsal filopodia onto the cell surface upon fixation, may be responsible for the localization data presented by Kwon and colleagues (2015). Second, our complementation data showed that Myo10's ability to interact with microtubules via its MyTH4 domain makes only a minor contribution to the myosin's ability to promote supernumerary centrosome clustering (possibility via its association with spindle microtubules). As to why Myo10's FERM domain-dependent interaction with ECM-bound integrins at the tips of retraction fibers is required for supernumerary centrosome clustering, we suggest that it serves as one of several anchors that together support HSET-dependent pole focusing by maintaining spindle tension (Krämer *et al.*, 2011; see Figure 8). By extension, we hypothesize that Myo10's FERM domain-dependent interaction with integrins promotes the dynein-dependent positioning of the mitotic spindle in exactly the same way (Thery and Bornens, 2006; Théry *et al.*, 2007; Iwano *et al.*, 2015). Finally, Myo10's role in supporting cell adhesion during mitosis may have added importance given that conventional focal adhesions largely disappear as cells enter mitosis (Dix *et al.*, 2018).

If not clustered, supernumerary centrosomes cause multipolar cell divisions that result in chromosome miss-segregation, aneuploidy and cell death (Godinho *et al.*, 2009; Cosenza and Krämer, 2016; Rhys and Godinho, 2017). Given this, and given that supernumerary centrosomes are rare in normal cells and common in cancer cells, drugs that inhibit the clustering of supernumerary centrosomes should selectively kill cancer cells. Indeed, compounds that inhibit HSET have been tested as anticancer therapeutics (Watts *et al.*, 2013). By the same token, a specific inhibitor of Myo10 might also serve to selectively kill cancer cells. Moreover, it might work synergistically with inhibitors of HSET. This seems likely given that assays quantifying the suppression of supernumerary centrosome clustering showed that actin disassembly was not synergistic with Myo10 KD (presumably because they act in the same pathway), but was synergistic with HSET inhibition (Kwon *et al.*, 2008). Notably, several recent studies have provided additional support for the idea that inhibitors of Myo10 might be effective as cancer therapeutics. First, Tokuo *et al.* (2018) reported that depletion of Myo10 in mouse models of melanoma reduces melanoma development and metastasis and extends medial survival time. Similarly, Kenchappa *et al.* (2020) reported that the lifespan of mice with glioblastoma is extended significantly on a Myo10 KO background. Third, Pozo *et al.* (2021) reported that the progression of breast cancer tumors in mice is inhibited by Myo10 depletion and accelerated by Myo10 overexpression. More generally, many cancer cell types exhibit elevated levels of Myo10, which may help support their growth by promoting the clustering of their extra centrosomes (Courson and Cheney, 2015; Jacquemet *et al.*, 2015; Hamidi and Ivaska, 2018). These and other studies (Jacquemet *et al.*, 2015), together with the data presented here, provide strong justification for performing screens to identify inhibitors of Myo10 as possible cancer therapeutics.

MATERIALS AND METHODS

Request a protocol through *Bio-protocol*.

Cell culture and transfection

HeLa cells (ATCC, CCL-2), HEK-293T cells (ATCC, CRL-3216), and primary MEFs were cultured in high glucose DMEM (Life Technologies) supplemented with 10% fetal bovine serum (FBS; Life Technologies) and Antibiotic-Antimycotic solution (Life Technologies) at 37°C in a 5% CO_2. MEFs were prepared from ~E19 embryos as described previously (Bockholt and Burridge, 1995). Only low passage number MEFs (<P3) were used for quantitating KO phenotypes. For imaging purposes, cells were cultured in coverglass bottom chamber slides (Cellvis) coated with fibronectin (10 ng/ml; Life Technologies). Cells were transfected using either Lipofectamine 3000 (Invitrogen) or an Amaxa nucleofection apparatus (Lonza) according to the manufacturer's instructions. For Myo10 KD, WT Hela cells were transfected with ON-TARGETplus human Myo10 siRNA-SMARTpool from Dharmacon (L-007217-00) using Lipofectamine RNAiMAX reagent (Invitrogen). To increase KD efficiency, transfection was performed twice in 2-d intervals and in reverse manner. The I bar-shaped fibronectin micropatterns were purchased from CYTOO and used according to the manufacturer's instructions. All cells were checked routinely by PCR for mycoplasma contamination.

Mice

WT C57BL/6 mice were purchased from Jackson Laboratories (#000664). The creation of the straight Myo10 KO mouse (tm1d) and the Myo10 cKO mouse (tm1c) was described previously (Heimsath *et al.*, 2017). Both KO strains are pure B6. All animal experiments were approved by the Animal Care and Use Committee of the National Heart, Lung, and Blood Institute, in accordance with the National Institutes of Health guidelines.

Antibodies and immunofluorescence

The following primary antibodies were used: mouse anti-γ-tubulin (MilliporeSigma, T6793, 1:300), mouse anti-α-tubulin (Abcam, ab7291, 1:300), rabbit anti-α-tubulin (Abcam, ab52866, 1:300), rabbit anti-myo10 (MilliporeSigma, HPA024223, 1:300), mouse anti-centrin1 (MilliporeSigma, 04-1624, 1:200), rabbit anti-centrin-1 (Abcam, ab101332, 1:200), rabbit anti-CDK5Rap2 (MilliporeSigma, 06-1398, 1:200), rabbit anti-pericentrin (Abcam, ab4448, 1:200), mouse anti-β-actin (Abcam, ab6276, 1:10,000), and mouse anti-Tpx2 (Santa Cruz Biotechnology, sc-53775, 1:200), rat-anti-CD29 (BD Pharmingen, 553715, 1:200). AlexaFluor-conjugated and HRP-conjugated secondary antibodies were purchased from Jackson ImmunoResearch Laboratories. DAPI, Alexa Fluor 488 labeled Phalloidin, and Alexa Fluor 568 labeled Phalloidin were purchased from ThermoFisher Scientific. Cells were fixed in 4% paraformaldehyde (PFA) for 10 min at RT unless subsequent staining was for centrosomes and pole-related proteins, in which case the cells were subjected to a two-step fixation method involving 1.5% PFA for 5 min followed by ice-cold MeOH for 5 min at –20°C. All PFA solutions were prepared in Cytoskeleton Stabilization Buffer (150 mM NaCl, 5 mM ethylene glycol-bis(β-aminoethyl ether)-*N*,*N*,*N*′,*N*′-tetraacetic acid (EGTA), 5 mM glucose, 5 mM $MgCl_2$, and 10 mM PIPES [pH 6.8]). Fixed cells were permeabilized and blocked by incubation for 15 min in phosphate-buffered saline (PBS) containing 0.15% Saponin and 5% FBS.

Fixed, permeabilized cells were incubated at RT for 1 h with primary and secondary antibodies diluted in blocking solution, with an intervening wash cycle using PBS.

DNA constructs, mutagenesis, and complementation

In Fusion HD cloning (Takara 638910) was used to move full length WT mouse Myo10 in EGFP-C1 to mScarlet-C1, and to clone WT and mutant versions of mScarlet-Myo10 into an Xlone plasmid (Addgene plasmid # 96930). The Xlone-GFP backbone plasmid was linearized by treating with restriction enzymes SpeI-HF (NEB R3133L) and KpnI-HF (NEB R3142L). To create the rescued cell lines, KO-1 cells were nucleofected using an Amaxa nucleofection apparatus (Lonza; program I-013) with Piggybac plasmid and either WT Xlone-mScarlet-Myo10 or mutant Xlone-mScarlet-Myo10. Cells were subsequently plated in three wells of a six-well plate and left to proliferate. At 90% confluency, cells were treated with 8 ug/ml blasticidin (Gold Biotechnology, B-800-100) for 48 h to select for cells that had integrated the Xlone-mScarlet-Myo10 plasmid. Afterward cells were left to proliferate in media without blasticidin, and 24 h before cell sorting were treated with 2 ug/ml doxycycline (Sigma-Aldrich, D9891-5G). Cells positive for mScarlet fluorescence were sorted, propagated and used in the rescue experiments. mScarlet tagged mut-FERM Myo10 was created by changing Ile 2041, which resides within the F3 lobe of Myo10's FERM domain, to Gln using PCR-based mutagenesis. The rationale for choosing this mutation to attenuate Myo10: integrin interaction is as follows: 1) the structure of the F3 lobe within the FERM domain of mouse talin 2 complexed with the cytoplasmic tail of human β1-integrin (PDB entry 3G9W), and the predicted structure of the complex between the F3 lobe within the FERM domain of human Myo10 (PDB entry 3AU5) and the cytoplasmic tail of human β1-integrin, align with a RMSD of ~1.2 Å (see *Materials and Methods* and Supplemental Figure S9 for details), 2) homologous hydrophobic residues in the C-terminal portion of talin's F3 lobe (mouse talin 2 residues W362, I395, I399, I402, and L403) and Myo10's F3 lobe (human Myo10 residues F2002, M2033, I2037, I2040, and V2041) make extensive interactions with the NPXY motif in the cytoplasmic tail of β1-integrin (Anthis *et al*., 2009), 3) changing Ile 396 in the F3 lobe of chicken talin (and only Ile 396) to an Ala reduces talin's affinity for β1-integrin by more than 10-fold (García-Alvarez *et al*., 2003), 4) Ile 396 in chicken talin corresponds to Ile 399 in mouse talin 2, Ile 2037 in human Myo10, and Ile 2041 in mouse Myo10 (the residue we mutated here to a Gln; see Supplemental Figure S9 for additional details). mScarlet tagged mut-MyTH4 Myo10 was created by changing four closely-spaced lysine residues present within the mouse Myo10 MyTH4 domain to glutamates (K1651, K1654, K1658, and K1661). This positively charged patch has been shown to bind to the acidic tails of α- and β-tubulin, and to be responsible for the ability of the MyTH4 domain to sediment with microtubules (Weber *et al*., 2004; Hirano *et al*., 2011). Of note, Kwon et al (Kwon *et al*., 2015) used human Myo10 in which two of these four lysines were changed to aspartates (K1647 and K1650, which correspond to K1651 and K1654 in mouse Myo10) to identify Myo10 functions that require interaction with microtubules. All clones were confirmed by sequencing.

Lentivirus packaging and cell transduction

The second generation lentiviral packaging plasmid psPAX2 (Addgene, #12260) was used to generate viral supernatants for pLenti-EB1-EGFP (Addgene, #118084), pLVX-FLAG-dTomato-centrin-1 (Addgene,#73332), pLentiPGK DEST H2B-iRFP670 (Addgene, 90237), pLV-RFP-H2B (Addgene, 26001), and pLenti-EGFP-Cre (Addgene, 86805). These plasmids were cotransfected with psPAX2 and pMD2.G (Addgene, #12259) into HEK-293T cells at ~80% confluency using LipoD293 (SignaGen, SL100668). Viral supernatants were collected 48 h posttransfection, clarified by centrifugation at 500 × g for 10 min, and concentrated using a Lenti-X concentrator (TakaraBio, #631231). Viral pellets were obtained by centrifugation of the concentrated virus at 1500 × g for 45 min at 4°C. The pellets were resuspended in complete DMEM and stored in aliquots at –80°C. Purified lentivirus was added directly to cells after the optimal amount was determined by a pilot experiment involving serial dilutions and determining the fraction of cells transduced. After a 6 h incubation, the cells were washed three times with PBS and returned to complete culture medium for imaging or fixation at various time points. To knock out Myo10 in MEFs isolated from the Myo10 cKO mouse (Heimsath *et al*., 2017), the cells were treated with lentivirus expressing EGFP-Cre as described above. Cell phenotypes were determined 48 h after lenti-cre transduction. All processes and materials were handled in accordance with the NIH biosafety guidelines.

Generation of Myo10-depleted HeLa cell clones using CRISPR

We used an online CRISPR design tool (http://cripr.mit.edu) to identify the following guide sequences within Exon 3 of human Myo10 (NCBI Reference Sequence: NC_000005.10): 5′-CACCGTATGCACCCCACGAACGAGG (PAM)-3′; 3′-CATACGTGGGGTGCTTGCTCCCAAA-5′. These guides sequences, which encode residues 57 to 62 (NHPTNE) in the 2058-residue human Myo10 heavy chain, were inserted into pSpCas9(BB)-2A-GFP (Addgene, #48138) to create pSpCas9(BB)-2A-GFP-ghMyo10 as described previously (Ran *et al*., 2013). Two days after Amaxa nucleofection of WT HeLa cells with pSpCas9(BB)-2A-GFP-ghMyo10, GFP-positive cells were subjected to single-cell sorting into 96-well plates using a BD FACS cell sorter, yielding two putative Myo10 KO clones (KO-1 and KO-2) from 384 wells. Sequencing of 12 PCR products generated using KO-1 genomic DNA and primers that span the guide sequence (KO-E3-F1: 5′-GGTATTCACTTACAAGCAGAGC-3′; KO-E3-R2: 5′-GCGTATTCACAAGCAGCAAGGTC-3′) revealed no WT sequence and roughly equal numbers of three mutations: 1) a frameshift mutation in which 125 nucleotides are inserted after the T codon in the gRNA sequence, leading to 25 out-of-frame amino acids followed by a stop codon, 2) a frameshift mutation in which the guide sequence is deleted and 158 nucleotides are inserted, leading to one out-of-frame amino acid followed by a stop codon, and 3) a missense mutation in which 18 nucleotides within the gRNA are deleted, leading to an in-frame deletion of residues NHPTNE. Similar to KO-1, sequencing of 12 PCR products generated using KO-2 genomic DNA revealed no WT sequence and roughly equal numbers of three mutations: 1) a frameshift mutation in which seven nucleotides within the gRNA sequence are deleted, leading to seven out-of-frame amino acids followed by a stop codon, 2) a frameshift mutation in which the gRNA sequence contains a five nucleotide deletion and a three nucleotide insertion, leading to four out-of-frame amino acids followed by a stop codon, and 3) a missense mutation in which 15 nucleotides within the gRNA are deleted, leading to an in-frame deletion of residues NHPTN. We conclude, therefore, that both KO lines contain no WT alleles, two nonsense/null alleles, and one missense allele that introduces six (KO-1) and 5 (KO-2) residue deletions in the motor domain.

Generation of Halo–Myo10 knock-in HeLa cells

The target guide sequence, which is immediately upstream of the start codon in human Myo10, was designed using an online CRISPR design tool provided by the Zhang lab at MIT (http://cripr.mit.edu):

5′ CACC GGAGCGGCACTCGGCGAGTC (PAM) 3′

3′ CCTCGCCGTGAGCCGCTCAGCAAA 5′

This guide sequence was cloned into pSPCas9(BB)-2A-puro(PX459)V2.0 (Addgene, #62988) as described previously (Ran *et al.*, 2013) to create pSPCas9(BB)-2A-puro(PX459)-hMyo10. To generate the donor plasmid, a gBlock was designed that contains two HDR (Homology Directed Repair) arms (560 bp 5′ HDR and 460 bp 3′ HDR), the target sequence with the mutation in the PAM site, a mutation to change the initiator methionine in Myo10 to an Alanine, and a multicloning site between the 5′and 3′ HDRs that contains an EcoRI site and an XhoI site. For cloning convenience, ~20 bp taken from the backbone of plasmid pSP72 (Promega, P2191) was added onto the outside end of both 5′ and 3′HDRs. Below is the complete gBlock sequence (the guide sequence is in bold, the EcoRI and XhoI sites are underlined, and the additional sequences from plasmid pSP72 are in italics).

*ACTGAGAGTGCACCATATG*AGAGCTGGCTGAGCCGCGGC-GCGGGACTGCTCACCTCCAAGCGCTCGCGCGGGGATCGCG-GCTCCTGCTCACTTTGCGGCCCGCTGTCCTCCTGCCCGCCCC-GAGGGCCCCCGGCCGGAGCGCAGAGGGAGGGGGCCGCGC TCGCCAGCACCCCGCCGCCTTCCCCCGCCTGGGGGAAGAAT GTGCCACCAGCTGTTCTCCGCTTGCGAGCGCTGCGCCCAGT AGTGAGGAACTTGGAGGAAGAAGAGACAAAGGCTGCCGTCG GGACGGGCGAGTTAGGGACTTGGGTTTGGGCGAA-CAAAAGGTGAGAAGGACAAGAAGGGACCGGGCGATGGCAG-CAGGGGAGCCCCGCGGGCGCGCGTCCTCGGGAGTGGCGC-CGTGACACGCATGGTTTCCCCGGACCCGCGGCGGCGCT-GACTTCCGCGAGTC**GGAGCGGCACTCGGCGAGTC**CCG-GACTGCGCTGGAACAGCTAGCGCTGAATTCGAGCTGTA-CAAGTCCGGACTCCTCGAGCCGGATAACTTCTTCACCGAGG-TAAGTGCGCTCCCAGTCCGACCTGGCCTCCG-GAGCCCAGGGAGAGAGGCGTCTGCCCACCACGCCGCGC-GCCCTGGGTACTTTTTCCTAAGCCCTGGAAGGCG-CAACTTTCTGGGAGTCTCCTGAAATCACCCCCCATCCCCCC-GCGGAGTCTCTGATGAGTAAGCCCGGGCAGGTTTTGTTTC-GTCCTGTCCCGCGCTCGCATTTTGCTCCGGGAGGTAGC-GAAGGTGCGTTTCCGTTTGCGTGGGTGGCTGGCTCTC-GGGGCGCCCTGGGACACCCGCGCCAGGTGA*AGATCTGCCG-GTCTCCCTATA*

This gBlock was cloned into pSP72 using an In-Fusion HD cloning protocol (TakaraBio) to create plasmid pSP72-hMyo10-KI. The Halo tag sequence starting with the methionine was then inserted into pSP72-hMyo10-KI using EcoRI and XhoI restriction sites to create the final donor construct, pSP72-Halo-hMyo10-KI. This plasmid and plasmid pSPCas9(BB)-2A-puro(PX459)-hMyo10 described above were transfected together into HeLa cells using Amaxa nucleofection (Lonza). Five days later the cells were subjected to single-cell sorting into 96-well plates. Several individual clones were analyzed by Western blotting and imaging following incubation for 1 h with the cell permeable JF-549 or JF-554 Halo dyes (Janelia/HHMI) at a final concentration of 200 nM.

Immunoblotting

Whole cell protein lysates were collected directly from culture dishes by adding 1X sodium dodecyl sulfate sample buffer, as described previously (Murugesan *et al.*, 2016). Samples were resolved on 4–12% or 6% NuPAGE Bis-Tris gels (Thermo Fisher Scientific) and transferred onto nitrocellulose membranes (Bio-Rad) using a semidry transfer system (Bio-Rad). Nitrocellulose membranes were blocked in TBST (10 mM Tris, pH 8.0, 150 mM NaCl, and 0.02% Tween 20) supplemented with 5% milk for 2 h, incubated with anti-Myo10 primary antibody overnight at 4°C, washed with TBST, and incubated in secondary antibody at RT for 2 h. Antibodies were diluted in TBST containing 5% milk. Actin detected using an anti-β-actin antibody was used as a loading control. Proteins were detected using SuperSignal West Pico Plus Chemiluminescent Substrate (Thermo Fisher Scientific) and quantitated using an Amersham Imager 600 (GE Healthcare Life Sciences).

Growth rate measurements

Primary MEFs isolated from WT C57BL/6 mouse embryos, non-exencephalic Myo10 KO mouse embryos (tm1d), and exencephalic Myo10 KO mouse embryos (tm1d) were seeded in individual wells of a six-well plate at 2.5×10^5 cells per well for the dense condition, 1.25×10^5 cells per well for the moderate condition, and 2.5×10^4 cells per well for the sparse condition. Cells were counted using Olympus Cell Counter model R1 after 3 d of culture.

Scoring mitotic phenotypes

To score mitotic phenotypes, HeLa cells (WT, KO-1, KO-2, Myo10 KD, and KO-1 rescued with pScarlet-Myo10) and MEFs (isolated from WT C57BL/6 mouse embryos, Myo10 KO mouse embryos (tm1d), and Myo10 cKO mouse embryos [tm1c, scored before and after treatment with pLenti-EGFP-Cre]) were plated in imaging chambers at moderate density, cultured overnight, fixed, and stained with anti-γ-tubulin, anti-α-tubulin and DAPI. Of note, cells were never synchronized for these studies. Z-stack images were taken in 0.25-µm steps. The criteria used to score metaphase cells as bipolar, semi-bipolar, or multipolar are described in the text. The same images were used to quantify the percent of cells exhibiting misaligned chromosomes and lagging chromosomes. Quantitation of the distance in Z between the two spindle poles in cells undergoing bipolar mitosis was based on the number of confocal slices between the γ-tubulin foci marking the two poles. To distinguish mitotic cells containing two centrosomes from mitotic cells containing supernumerary centrosomes, and to distinguish γ-tubulin-positive poles containing two centrioles from those containing one centriole or no centriole, metaphase cells were stained with anti-γ-tubulin, anti-centrin-1, and DAPI. To gauge pole maturation, cells were fixed and stained with anti-CDK5Rap2, anti-centrin-1, and DAPI. Cells with a normal number of centrosomes were imaged in 0.25-µm steps, and the total intensity of CDK5Rap2 per pole was determined by summing slices, then thresholding using the OTSU function in Image J.

Dynamic imaging of acentriolar spindle poles using GFP-EB1

Myo10-depleted HeLa cells transduced with pLenti-EB1-EGFP, pLVX-FLAG-dTomato-centrin-1, and pLentiPGK DEST H2B-iRFP670, or pLenti-EB1-EGFP and pLenti-RFP-H2B, were imaged live on an Airyscan 880 microscope equipped with a 60X, 1.4 NA objective (one frame every 2 s for 2 min).

Modeling the interaction between the F3 lobe in Myo10's FERM domain and the cytoplasmic tail of β1-integrin

To predict the interaction between the F3 lobe within the FERM domain of human Myo10 (PDB entry 3AU5) and the cytoplasmic tail of human β1-integrin, we used PyMOL (Schrödinger, 2015) to superimpose the F3 lobe of human Myo10 with the structure of the F3 lobe within the FERM domain of mouse talin 2 FERM domain complexed with the cytoplasmic tail of human β1-integrin (PDB entry 3g9w). F3 lobe residues Y1953 to S2046 in Myo10 and Y311 to S408 in talin 2, and residues G750 to N788 in the β1-integrin cytoplasmic tail, were included in the structural prediction.

Imaging and statistical analyses

Imaging of both fixed and live cells was performed on a Zeiss Airyscan 880 microscope equipped with a 60X, 1.4 NA objective. Images were processed in auto strength mode using ZenBlack software (Version 2.3) and analyzed using ImageJ. Excel or GraphPad Prism were used for statistical analyses and graphing. Statistical significance was determined using unpaired *t* test and indicated as follows: * = $P < 0.05$, ** = $P < 0.01$, *** = $P < 0.001$, and **** = $P < 0.0001$.

ACKNOWLEDGMENTS

This work was supported by the Intramural Research Program of the National Heart, Lung, and Blood Institute (1ZIAHL000514-31 to J.A.H.) and by R01GM134531 to R.E.C. The authors are very grateful to Mingjie Zhang (HK University of Science and Technology, Hong Kong) for his suggestion to mutate Ile 2041 in mouse Myo10 to attenuate its interaction with integrin. The authors also thank Nasser Rusan (NHLBI, National Institutes of Health), Jadranka Loncarek (NCI, National Institutes of Health), and Jeffrey B. Woodruff (UT Southwestern) for their expert advice.

REFERENCES

Albuschies J, Vogel V (2013). The role of filopodia in the recognition of nanotopographies. Sci Rep 3, 1–9.

Alieva N, Efremov A, Hu S, Oh D, Chen Z, Natarajan M, Ong H, Jegou A, Romet-Lemonne G, Groves J (2019). Myosin IIA and formin dependent mechanosensitivity of filopodia adhesion. Nat Commun 10, 3593.

Anthis NJ, Wegener KL, Ye F, Kim C, Goult BT, Lowe ED, Vakonakis I, Bate N, Critchley DR, Ginsberg MH (2009). The structure of an integrin/talin complex reveals the basis of inside-out signal transduction. EMBO J 28, 3623–3632.

Baboolal TG, Mashanov GI, Nenasheva TA, Peckham M, Molloy JE (2016). A combination of diffusion and active translocation localizes myosin 10 to the filopodial tip. J Biol Chem 291, 22373–22385.

Berg JS, Cheney RE (2002). Myosin-X is an unconventional myosin that undergoes intrafilopodial motility. Nat Cell Biol 4, 246–250.

Berg JS, Derfler BH, Pennisi CM, Corey DP, Cheney RE (2000). Myosin-X, a novel myosin with pleckstrin homology domains, associates with regions of dynamic actin. J Cell Sci 113, 3439–3451.

Beskow LM (2016). Lessons from HeLa cells: the ethics and policy of biospecimens. Annu Rev Genomics Hum Genet 17, 395–417.

Bockholt SM, Burridge K (1995). An examination of focal adhesion formation and tyrosine phosphorylation in fibroblasts isolated from src, fyn, and yes mice. Cell Adhes Commun 3, 91–100.

Bohil AB, Robertson BW, Cheney RE (2006). Myosin-X is a molecular motor that functions in filopodia formation. Proc Natl Acad Sci USA 103, 12411–12416.

Bornschlögl T, Romero S, Vestergaard CL, Joanny J-F, Van Nhieu GT, Bassereau P (2013). Filopodial retraction force is generated by cortical actin dynamics and controlled by reversible tethering at the tip. Proc Natl Acad Sci USA 110, 18928–18933.

Cosenza MR, Krämer A (2016). Centrosome amplification, chromosomal instability and cancer: mechanistic, clinical and therapeutic issues. Chromosome Res 24, 105–126.

Courson DS, Cheney RE (2015). Myosin-X and disease. Exp Cell Res 334, 10–15.

Cramer L, Mitchison TJ (1993). Moving and stationary actin filaments are involved in spreading of postmitotic PtK2 cells. J Cell Biol 122, 833–843.

Cramer LP, Mitchison TJ (1995). Myosin is involved in postmitotic cell spreading. J Cell Biol 131, 179–189.

Cramer LP, Mitchison TJ (1997). Investigation of the mechanism of retraction of the cell margin and rearward flow of nodules during mitotic cell rounding. Mol Biol Cell 8, 109–119.

Dickinson ME, Flenniken AM, Ji X, Teboul L, Wong MD, White JK, Meehan TF, Weninger WJ, Westerberg H, Adissu H (2016). High-throughput discovery of novel developmental phenotypes. Nature 537, 508–514.

Dix CL, Matthews HK, Uroz M, McLaren S, Wolf L, Heatley N, Win Z, Almada P, Henriques R, Boutros M (2018). The role of mitotic cell-substrate adhesion re-modeling in animal cell division. Dev Cell 45, 132–145. e133.

Fischer RS, Lam P-Y, Huttenlocher A, Waterman CM (2019). Filopodia and focal adhesions: An integrated system driving branching morphogenesis in neuronal pathfinding and angiogenesis. Dev Biol 451, 86–95.

Gallop JL (2020). Filopodia and their links with membrane traffic and cell adhesion. Semin Cell Dev Biol, 102, 81–89.

García-Alvarez B, de Pereda JM, Calderwood DA, Ulmer TS, Critchley D, Campbell ID, Ginsberg MH, Liddington RC (2003). Structural determinants of integrin recognition by talin. Mol Cell 11, 49–58.

Godinho SA, Kwon M, Pellman D. (2009). Centrosomes and cancer: How cancer cells divide with too many centrosomes. Cancer Metastasis Rev 28, 85–98.

Hamidi H, Ivaska J (2018). Every step of the way: Integrins in cancer progression and metastasis. Nat Rev Cancer 18, 533–548.

Hammers DW, Hart CC, Matheny MK, Heimsath EG, il Lee Y, Hammer III, JA, Cheney RE, Sweeney HL. (2021). Filopodia powered by class x myosin promote fusion of mammalian myoblasts. eLife 10, e72419.

He K, Sakai T, Tsukasaki Y, Watanabe TM, Ikebe M (2017). Myosin X is recruited to nascent focal adhesions at the leading edge and induces multi-cycle filopodial elongation. Sci Rep 7, 13685.

Heimsath Jr, EG, Yim Y-I, Mustapha M, Hammer JA, Cheney RE. (2017). Myosin-X knockout is semi-lethal and demonstrates that myosin-X functions in neural tube closure, pigmentation, hyaloid vasculature regression, and filopodia formation. Sci Rep 7, 17354.

Hirano Y, Hatano T, Takahashi A, Toriyama M, Inagaki N, Hakoshima T (2011). Structural basis of cargo recognition by the myosin-X MyTH4–FERM domain. EMBO J 30, 2734–2747.

Horsthemke M, Bachg AC, Groll K, Moyzio S, Müther B, Hemkemeyer SA, Wedlich-Söldner R, Sixt M, Tacke S, Bähler M (2017). Multiple roles of filopodial dynamics in particle capture and phagocytosis and phenotypes of Cdc42 and Myo10 deletion. J Biol Chem 292, 7258–7273.

Houdusse A, Titus MA (2021). The many roles of myosins in filopodia, microvilli and stereocilia. Curr Biol 31, R586–R602.

Hu W, Wehrle-Haller B, Vogel V (2014). Maturation of filopodia shaft adhesions is upregulated by local cycles of lamellipodia advancements and retractions. PLoS One 9, e107097.

Iwano S, Satou A, Matsumura S, Sugiyama N, Ishihama Y, Toyoshima F (2015). PCTK1 regulates integrin-dependent spindle orientation via protein kinase A regulatory subunit KAP0 and myosin X. Mol Cell Biol 35, 1197–1208.

Jacquemet G, Hamidi H, Ivaska J (2015). Filopodia in cell adhesion, 3D migration and cancer cell invasion. Curr Opin Cell Biol 36, 23–31.

Jacquemet G, Baghirov H, Georgiadou M, Sihto H, Peuhu E, Cettour-Janet P, He T, Perälä M, Kronqvist P, Joensuu H (2016). L-type calcium channels regulate filopodia stability and cancer cell invasion downstream of integrin signalling. Nat Commun 7, 13297.

Jacquemet G, Stubb A, Saup R, Miihkinen M, Kremneva E, Hamidi H, Ivaska J (2019). Filopodome mapping identifies p130Cas as a mechanosensitive regulator of filopodia stability. Curr Biol 29, 202–216. e207.

Johnson HE, King SJ, Asokan SB, Rotty JD, Bear JE, Haugh JM (2015). F-actin bundles direct the initiation and orientation of lamellipodia through adhesion-based signaling. J Cell Biol 208, 443–455.

Kenchappa RS, Mistriotis P, Wisniewski E, Bhattacharya S, Kulkarni T, West R, Luu A, Conlon M, Heimsath E, Crish JF (2020). Myosin 10 regulates invasion, mitosis, and metabolic signaling in glioblastoma. iScience 23, 101802.

Kerber ML, Cheney RE (2011). Myosin-X: A MyTH-FERM myosin at the tips of filopodia. J Cell Sci 124, 3733–3741.

Kerber ML, Jacobs DT, Campagnola L, Dunn BD, Yin T, Sousa AD, Quintero OA, Cheney RE (2009). A novel form of motility in filopodia revealed by imaging myosin-X at the single-molecule level. Curr Biol 19, 967–973.

Kita AM, Swider ZT, Erofeev I, Halloran MC, Goryachev AB, Bement WM (2019). Spindle–F-actin interactions in mitotic spindles in an intact vertebrate epithelium. Mol Biol Cell 30, 1645–1654.

Krämer A, Maier B, Bartek J (2011). Centrosome clustering and chromosomal (in) stability: A matter of life and death. Mol Oncol 5, 324–335.

Kwon M, Godinho SA, Chandhok NS, Ganem NJ, Azioune A, Thery M, Pellman D. (2008). Mechanisms to suppress multipolar divisions in cancer cells with extra centrosomes. Genes Dev 22, 2189–2203.

Kwon M, Bagonis M, Danuser G, Pellman D. (2015). Direct microtubule-binding by myosin-10 orients centrosomes toward retraction fibers and subcortical actin clouds. Dev Cell 34, 323–337.

Lagarrigue F, Vikas Anekal P, Lee H-S, Bachir AI, Ablack JN, Horwitz AF, Ginsberg MH (2015). A RIAM/lamellipodin–talin–integrin complex forms the tip of sticky fingers that guide cell migration. Nat Commun 6, 8492.

Leijnse N, Oddershede LB, Bendix PM (2015). Helical buckling of actin inside filopodia generates traction. Proc Natl Acad Sci USA 112, 136–141.

Liu R, Billington N, Yang Y, Bond C, Hong A, Siththanandan V, Takagi Y, Sellers JR (2021). A binding protein regulates myosin-7a dimerization and actin bundle assembly. Nat Commun 12, 563.
Maiato H, Logarinho E (2014). Mitotic spindle multipolarity without centrosome amplification. Nat Cell Biol 16, 386–394.
Miihkinen M, Grönloh ML, Popović A, Vihinen H, Jokitalo E, Goult BT, Ivaska J, Jacquemet G (2021). Myosin-X and talin modulate integrin activity at filopodia tips. Cell Rep 36, 109716.
Mitchison TJ (1992). Actin based motility on retraction fibers in mitotic PtK2 cells. Cell Motil Cytoskeleton 22, 135–151.
Morgan MR, Byron A, Humphries MJ, Bass MD (2009). Giving off mixed signals—distinct functions of α5β1 and αvβ3 integrins in regulating cell behaviour. IUBMB Life 61, 731–738.
Murugesan S, Hong J, Yi J, Li D, Beach JR, Shao L, Meinhardt J, Madison G, Wu X, Betzig E (2016). Formin-generated actomyosin arcs propel T cell receptor microcluster movement at the immune synapse. J Cell Biol 215, 383–399.
Nagy S, Ricca BL, Norstrom MF, Courson DS, Brawley CM, Smithback PA, Rock RS (2008). A myosin motor that selects bundled actin for motility. Proc Natl Acad Sci USA 105, 9616–9620.
Pi X, Ren R, Kelley R, Zhang C, Moser M, Bohil AB, DiVito M, Cheney RE, Patterson C (2007). Sequential roles for myosin-X in BMP6-dependent filopodial extension, migration, and activation of BMP receptors. J Cell Biol 179, 1569–1582.
Plantard L, Arjonen A, Lock JG, Nurani G, Ivaska J, Strömblad S (2010). PtdIns (3, 4, 5) P 3 is a regulator of myosin-X localization and filopodia formation. J Cell Sci 123, 3525–3534.
Pozo MF, Geng X, Tamagno I, Jackson MW, Heimsath EG, Hammer JA, Cheney RE, Zhang Y (2021). MYO10 drives genomic instability and inflammation in cancer. Sci Adv 7, eabg6908.
Raines AN, Nagdas S, Kerber ML, Cheney RE (2012). Headless Myo10 is a negative regulator of full-length Myo10 and inhibits axon outgrowth in cortical neurons. J Biol Chem 287, 24873–24883.
Ran FA, Hsu PD, Wright J, Agarwala V, Scott DA, Zhang F (2013). Genome engineering using the CRISPR-Cas9 system. Nat Protoc 8, 2281–2308.
Rhys AD, Godinho SA (2017). Dividing with extra centrosomes: A double edged sword for cancer cells. Adv Exp Med Biol 1002, 47–67.
Ricca BL, Rock RS (2010). The stepping pattern of myosin X is adapted for processive motility on bundled actin. Biophys J 99, 1818–1826.
Romero S, Quatela A, Bornschlögl T, Guadagnini S, Bassereau P, Tran Van Nhieu G (2012). Filopodium retraction is controlled by adhesion to its tip. J Cell Sci 125, 4999–5004.
Ropars V, Yang Z, Isabet T, Blanc F, Zhou K, Lin T, Liu X, Hissier P, Samazan F, Amigues B. (2016). The myosin X motor is optimized for movement on actin bundles. Nat Commun 7, 12456.
Schäfer C, Borm B, Born S, Möhl C, Eibl E-M, Hoffmann B (2009). One step ahead: role of filopodia in adhesion formation during cell migration of keratinocytes. Exp Cell Res 315, 1212–1224.
Schrödinger L (2015). The PyMOL molecular graphics system, version 1.8. (No Title).
Singh SK, Kurfurst R, Nizard C, Schnebert S, Perrier E, Tobin DJ (2010). Melanin transfer in human skin cells is mediated by filopodia—A model for homotypic and heterotypic lysosome-related organelle transfer. FASEB J 24, 3756–3769.
Sousa AD, Cheney RE (2005). Myosin-X: A molecular motor at the cell's fingertips. Trends Cell Biol 15, 533–539.
Taubenberger AV, Baum B, Matthews HK (2020). The mechanics of mitotic cell rounding. Front Cell Dev Biol 8, 687.
Thery M, Bornens M (2006). Cell shape and cell division. Curr Opin Cell Biol 18, 648–657.
Théry M, Jiménez-Dalmaroni A, Racine V, Bornens M, Jülicher F (2007). Experimental and theoretical study of mitotic spindle orientation. Nature 447, 493–496.
Tokuo H (2020). Myosin X. Myosins: A Superfamily of Molecular Motors, 391–403.
Tokuo H, Katsuhide M, Mitsuo I. (2007). The motor activity of myosin-X promotes actin fiber convergence at the cell periphery to initiate filopodia formation. J Cell Biol 179, 229–238.
Tokuo H, Bhawan J, Coluccio LM (2018). Myosin X is required for efficient melanoblast migration and melanoma initiation and metastasis. Sci Rep 8, 10449.
Toyoshima F, Nishida E (2007). Integrin-mediated adhesion orients the spindle parallel to the substratum in an EB1-and myosin X-dependent manner. EMBO J 26, 1487–1498.
Umeki N, Jung HS, Sakai T, Sato O, Ikebe R, Ikebe M (2011). Phospholipid-dependent regulation of the motor activity of myosin X. Nat Struct Mol Biol 18, 783–788.
Varadarajan R, Rusan NM (2018). Bridging centrioles and PCM in proper space and time. Essays Biochem 62, 793–801.
Vasquez-Limeta A, Loncarek J (2021). Human centrosome organization and function in interphase and mitosis. Semin Cell Dev Biol, 117, 30–41.
Watts CA, Richards FM, Bender A, Bond PJ, Korb O, Kern O, Riddick M, Owen P, Myers RM, Raff J (2013). Design, synthesis, and biological evaluation of an allosteric inhibitor of HSET that targets cancer cells with supernumerary centrosomes. Chem Biol 20, 1399–1410.
Weber KL, Sokac AM, Berg JS, Cheney RE, Bement WM (2004). A microtubule-binding myosin required for nuclear anchoring and spindle assembly. Nature 431, 325–329.
Weck ML, Grega-Larson NE, Tyska MJ (2017). MyTH4-FERM myosins in the assembly and maintenance of actin-based protrusions. Curr Opin Cell Biol 44, 68–78.
Wong S, Guo W-H, Wang Y-L (2014). Fibroblasts probe substrate rigidity with filopodia extensions before occupying an area. Proc Natl Acad Sci USA 111, 17176–17181.
Woolner S, O'Brien LL, Wiese C, Bement WM (2008). Myosin-10 and actin filaments are essential for mitotic spindle function. J Cell Biol 182, 77–88.
Zhang H, Berg JS, Li Z, Wang Y, Lång P, Sousa AD, Bhaskar A, Cheney RE, Strömblad S (2004). Myosin-X provides a motor-based link between integrins and the cytoskeleton. Nat Cell Biol 6, 523–531.